Water Resources Research

RESEARCH ARTICLE
10.1029/2025WR040749

Detecting Morphological Change From DInSAR Data in Ephemeral, Braided, Gravel Bed Rivers. Application to the Ungauged Trionto River, Italy

Valeria Guadagno[1,2], Giuseppe Del Giudice[3], Cristiana Di Cristo[3], Diego Di Martire[4], Angelo Leopardi[1], Matthew J. Czapiga[2,5], and Enrica Viparelli[2,4]

[1]Dipartimento di Ingegneria Civile e Meccanica, Università degli Studi di Cassino e del Lazio Meridionale, Cassino, Italy, [2]Department of Civil and Environmental Engineering, University of South Carolina, Columbia, SC, USA, [3]Dipartimento di Ingegneria Civile, Edile ed Ambientale, Università degli Studi di Napoli Federico II, Naples, Italy, [4]Dipartimento di Scienze della Terra, dell'Ambiente e delle Risorse, Università degli Studi di Napoli Federico II, Naples, Italy, [5]School of Science and Engineering, Tulane University, New Orleans, LA, USA

Key Points:

- Morphological change (active width and number of active branches) in a braided, gravel bed river is estimated from Differential Interferometry of Synthetic Aperture Radar data
- The analysis predicts morphological change increasing with valley width and discharge magnitude in agreement with previous studies
- Comparison with optical and multispectral images indicates that this analysis can reasonably identify active channel location

Supporting Information:

Supporting Information may be found in the online version of this article.

Correspondence to:

C. Di Cristo,
cristiana.dicristo@unina.it

Citation:

Guadagno, V., Del Giudice, G., Di Cristo, C., Di Martire, D., Leopardi, A., Czapiga, M. J., & Viparelli, E. (2026). Detecting morphological change from DInSAR data in ephemeral, braided, gravel bed rivers. application to the ungauged Trionto River, Italy. *Water Resources Research*, *62*, e2025WR040749. https://doi.org/10.1029/2025WR040749

Received 7 APR 2025
Accepted 19 DEC 2025

Author Contributions:

Conceptualization: Valeria Guadagno, Giuseppe Del Giudice, Cristiana Di Cristo, Diego Di Martire, Angelo Leopardi, Enrica Viparelli
Data curation: Valeria Guadagno, Diego Di Martire, Matthew J. Czapiga
Formal analysis: Valeria Guadagno, Enrica Viparelli
Funding acquisition: Angelo Leopardi

Abstract Estimating morphological change in braided gravel bed rivers is important to determine the geometry of the active part of the braidplain, that is the width of the area where bed material is transported and the number of active branches during a certain time interval. Repeated surveys and photogrammetry have been used to measure morphological change with different spatial and temporal resolution but characterizing the geometry of braided rivers remains a problem. Increased satellite coverage and frequency of revisiting times motivated satellite-based studies of river dynamics. Here we present a procedure to estimate morphological change in ephemeral, braided, gravel bed rivers from Differential Interferometry of Synthetic Aperture Radar (DInSAR) data conducted on Sentinel-1 SAR images, that is information on areas where ground displacement larger than 5–6 cm occurred. We hypothesize that such displacement is representative of bedload transport and can be used to describe the morphologically active braidplain. The procedure is applied to the Trionto River in Southern Italy. Results indicate that the proposed approach has the potential to capture different channel dynamics related to lateral confinement and flood hydrographs. In agreement with field and laboratory observations reported in the literature, narrower morphological active width and fewer active branches are estimated where the valley is most confined. In response to a relatively frequent flood, active width remains independent of lateral confinement and one or two active branches are predicted. Conversely, a large, less frequent flood results in the reorganization of the channel network with comparatively larger active width and more active branches in the widest portion of the braidplain.

Plain Language Summary Rivers can be described based on their planform shape, that is the shape we see when we look at them from higher ground or from an airplane. Main feature of a braided river is the presence of several channels (braids) that surround islands, which may or may not be vegetated. During floods just one or two braids typically transport sediment at a given point in time (active braids). Sediment erosion and deposition from and to the sides of an active braid channel may result in lateral displacement of the braid and/or in the formation of a new active braid. Measuring the width of the active area and the number of braids that transported sediment during a flood remains a problem. Here we illustrate how the analysis of satellite data indicating ground movement has the potential to help estimate active width and number of channels in ephemeral, braided, gravel bed rivers.

1. Introduction

Predicting the geometry of alluvial rivers is a long-standing problem with applications to flood protection, river management and restoration (e.g., Bertoldi, Zanoni, & Tubino, 2009; Carbonari et al., 2020; Misset et al., 2020). Regime-type relations and physics-based modeling have been widely used to describe at-a-station and downstream hydraulic geometry of single thread rivers in terms of bankfull width, depth and discharge (e.g., Czapiga et al., 2019; Dunne et al., 2018; Dunne & Jerolmack, 2020; Leopold & Maddock, 1953; Li et al., 2015; Parker, 1979; Parker et al., 2007; Trampush et al., 2014; Viparelli & Eke, 2021; Wilkerson & Parker, 2011).

Defining formative conditions and channel geometry in braided rivers is more difficult than in single thread rivers due to the coexistence of multiple spatial scales and to the rapidly evolving geometry (Bertoldi et al., 2010; Egozi

Methodology: Valeria Guadagno, Cristiana Di Cristo, Diego Di Martire, Angelo Leopardi, Matthew J. Czapiga, Enrica Viparelli
Project administration: Giuseppe Del Giudice, Angelo Leopardi
Software: Valeria Guadagno, Diego Di Martire, Matthew J. Czapiga
Supervision: Giuseppe Del Giudice, Cristiana Di Cristo, Enrica Viparelli
Validation: Valeria Guadagno, Matthew J. Czapiga
Writing – original draft: Valeria Guadagno, Giuseppe Del Giudice, Diego Di Martire, Angelo Leopardi, Matthew J. Czapiga, Enrica Viparelli
Writing – review & editing: Valeria Guadagno, Giuseppe Del Giudice, Cristiana Di Cristo, Diego Di Martire, Angelo Leopardi, Matthew J. Czapiga, Enrica Viparelli

& Ashmore, 2009; Paola, 2001; Rhoads, 2020), which make measurement of channel topography and sediment fluxes challenging (Ashmore & Church, 1998; Ashmore & Sauks, 2006; Carson & Griffiths, 1989; Ferguson, 1993). The geometry of a braided, gravel bed river is often described in terms of wetted and active geometries. Wetted width and depth correspond to average values of the cross section occupied by water. Active width, depth and band describe the average geometry of the cross section where bedload transport occurs (e.g., Ashmore, 1991a, 1991b, 2013; Egozi & Ashmore, 2008; García-Martínez & Rinaldi, 2022), which is typically smaller than the wetted cross section in gravel bed rivers.

With the increase in satellite coverage and frequency of revisiting times, researchers have been exploring the use of multispectral and Synthetic Aperture Radar, SAR, data to study river dynamics. In this paper we consider research on braided, gravel bed rivers only. The pioneering work by Smith et al. (1996) illustrates how SAR images collected by the First European Remote Sensing Satellite ERS 1 (25 m ground resolution) can be used to estimate discharge and wetted geometry in ungauged rivers. Rossi et al. (2023) integrated publicly available Sentinel-1 SAR images with measurements of flow rate on the perennial, gravel bed Tagliamento River, Italy, to estimate wetted geometry and erosion of individual channel branches. Crivellaro et al. (2024) estimated active channel geometries and lateral movement from Landsat and Sentinel-2 multi-spectral medium-resolution (10 m) satellite images on the perennial Tagliamento, Skumbin and Vyosa rivers.

A common feature of these studies is the distinction between inundated and emergent portions of the braidplain, which is effective for perennial rivers because satellite images capture both high and low flow periods. The approach, however, is inadequate to study ephemeral streams, such as those in the Mediterranean basin, where floods are rapid and short (C. Viparelli & Viparelli, 1979, Hassan, 1990, 2005, Laronne & Reid, 1993, Laronne et al., 1994, Hassan et al., 2006, 2009, Cohen & Laronne, 2005, Calle et al., 2020, Conesa-Garcia et al., 2022).

In this paper, we propose to detect morphological change and estimate active width of ephemeral, braided, gravel bed rivers from SAR data. We use Differential Interferometry of Synthetic Aperture Radar data (DInSAR) (Gabriel et al., 1989), by processing C-band radar images from the European Space Agency SENTINEL-1 constellation, with a revisiting time of 6 days, acquired as part of the Copernicus Project. DInSAR is a technique to produce displacement rate maps and time series of displacements with sub-centimeter precision (Colesanti & Wasowski, 2006). Typical targets of the analysis are buildings, structures and rocks, which maintain a constant electromagnetic response (called phase) to the signals sent over time. In particular, DInSAR technique can be of aid in monitoring target movements that do not exceed half the wavelength of the images, which in our case is approximately 5–6 cm because the images were processed in the C-band (Franceschetti et al., 1992). Shifts greater than half the wavelength between two acquisitions (5–6 cm) would cause a reduction in phase quality, making it impossible to monitor these areas.

The proposed methodology uses the Permanent Scatter Technique, described in Colesanti et al. (2003), based on a long temporal series of interferometric data. Only scatterers slightly affected by temporal and geometrical decorrelation are selected (Ferretti et al., 2000). The stable targets, called Permanent Scatter (PS), are detected based on a statistical analysis on the amplitudes of the electromagnetic returns. Approximately 20–30 images are required to properly identify PSs with statistical indices and guarantee a correct application of the interferometric technique (Colesanti & Wasowski, 2006). The minimum duration of the data collection period then depends on the satellite visitation frequency of a given location.

We hypothesize that the lack of measurable displacement in a braidplain, combined with the absence of PSs, indicates that ground movement between consecutive acquisitions was too large to be detected. Therefore, the absence of PS is interpreted as evidence of significant morphological change (Ferretti et al., 2001). Conversely, the presence of permanent scatters indicates absence of morphological change and the lack of significant gravel movement. We test this hypothesis on a 5 km long reach of the ungauged Trionto River in Southern Italy. The study site was chosen because it has a natural hydrologic regime and for the availability of a rainfall measuring station and granulometric data (Viparelli, C. 1964). Moreover, braidplain width at this site varies considerably over the relatively short distance providing the possibility to consider river segments subjected to very similar hydrographs and different valley confinement (Carbonari et al., 2020; Garcia Lugo et al., 2015).

This manuscript is organized as follows. We describe the study area in Section 2, present materials and methods in Section 3. The application to the Trionto River is presented in Section 4 and results are discussed in Section 5.

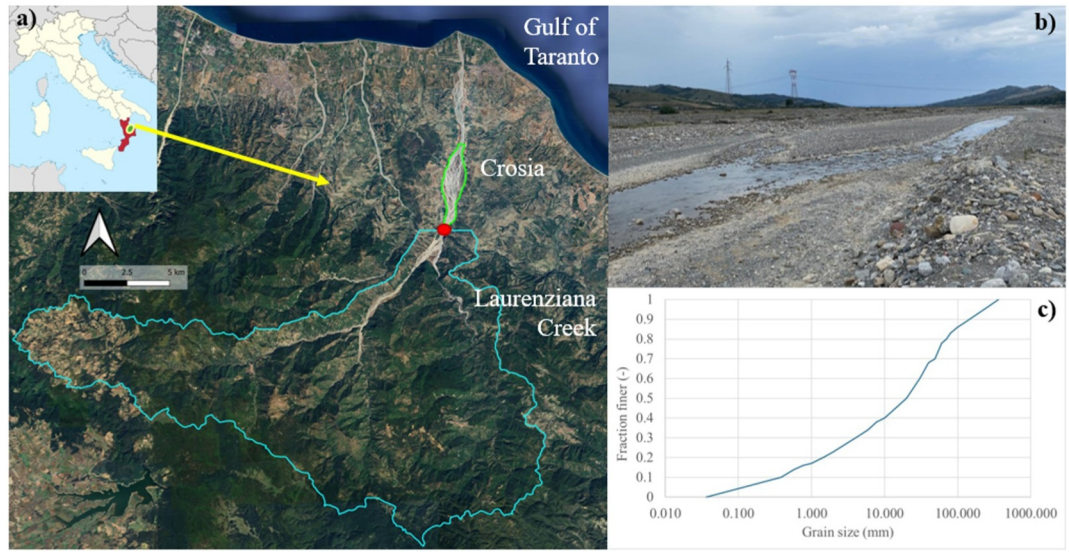

Figure 1. Description of the study site (a) Google Map image with location of the study site (area in the green perimeter), the Cropalati bridge (red dot) and the catchment upstream of the bridge (area in blue perimeter). (b) Picture of the unarmored gravel bed taken in June 2024. (c) Grain size distribution of the Trionto bed material.

2. Study Area

The Trionto is an ephemeral River located in Calabria, a region in Southern Italy (Figure 1a). Trionto headwaters are in Sila mountains and the river flows into the Gulf of Taranto. The 5 km long study reach (green in Figure 1a) corresponds to a mostly undisturbed portion of the braidplain (Figure 1b). The upstream section is located at the national road SS531 bridge (Cropalati bridge, red dot in Figure 1a), immediately downstream of the confluence with Laurenzana Creek, and the downstream end is immediately upstream of the town of Crosia. Catchment area A at the Cropalati bridge is 262 km^2.

Braidplain width varies between 200 m and 1.3 km. This change in channel confinement is common to gravel bed rivers in the region, and it is typically associated with changes in channel morphology and slope. In particular, planform configuration can transition from single thread with alternate bars in the narrowest reaches to braided where the valley widens (C. Viparelli, 1972). Braidplain slope is estimated from a Digital Terrain Model (DTM) with a resolution of 5 m × 5 m generated by the Calabria flight in 2007–2008 and resampled with the bicubic interpolation method. Slope at the study site ranges between 0.7% in the upstream narrow section to 1.5% in the wide downstream part.

Sediment in the study domain originates from a gravel source area immediately upstream of the Cropalati bridge (marked with a red dot in Figure 1a) and consists of a mixture of gravel and sand shown in Figures 1b and 1c with geometric mean grain size D_g equal to 11 mm. Mean grain size therefore corresponds to twice the maximum displacement measurable from DInSAR data. Median grain size is D_{50} = 20 mm and 84% and 90% of the sediment is finer than D_{84} = 80 mm and D_{90} = 130 mm, respectively (Figure 1c). The volume fraction content of sand is 25% (C. Viparelli, 1964). Flows that can transport bedload and cause morphological change are initiated by rainfall events (Versace et al., 1989). As spring contribution to the Trionto River is minimal (C. Viparelli & Viparelli, 1979), the Trionto River is unarmored, similar to other ephemeral streams in the Mediterranean basin (e.g., Hassan, 2005; Laronne & Reid, 1993).

Continuous measurement of flow discharge in braided rivers is difficult because of the unstable nature of the channel network (Ashmore & Sauks, 2006). For this reason, the regional agency collecting water data, ARPACAL, does not measure stage or discharge on the Trionto River. The agency maintains, however, a rain gage close to the Cropalati bridge (red dot in Figure 1a) that we use to identify rainfall events that may generate floods and morphological change in the study reach.

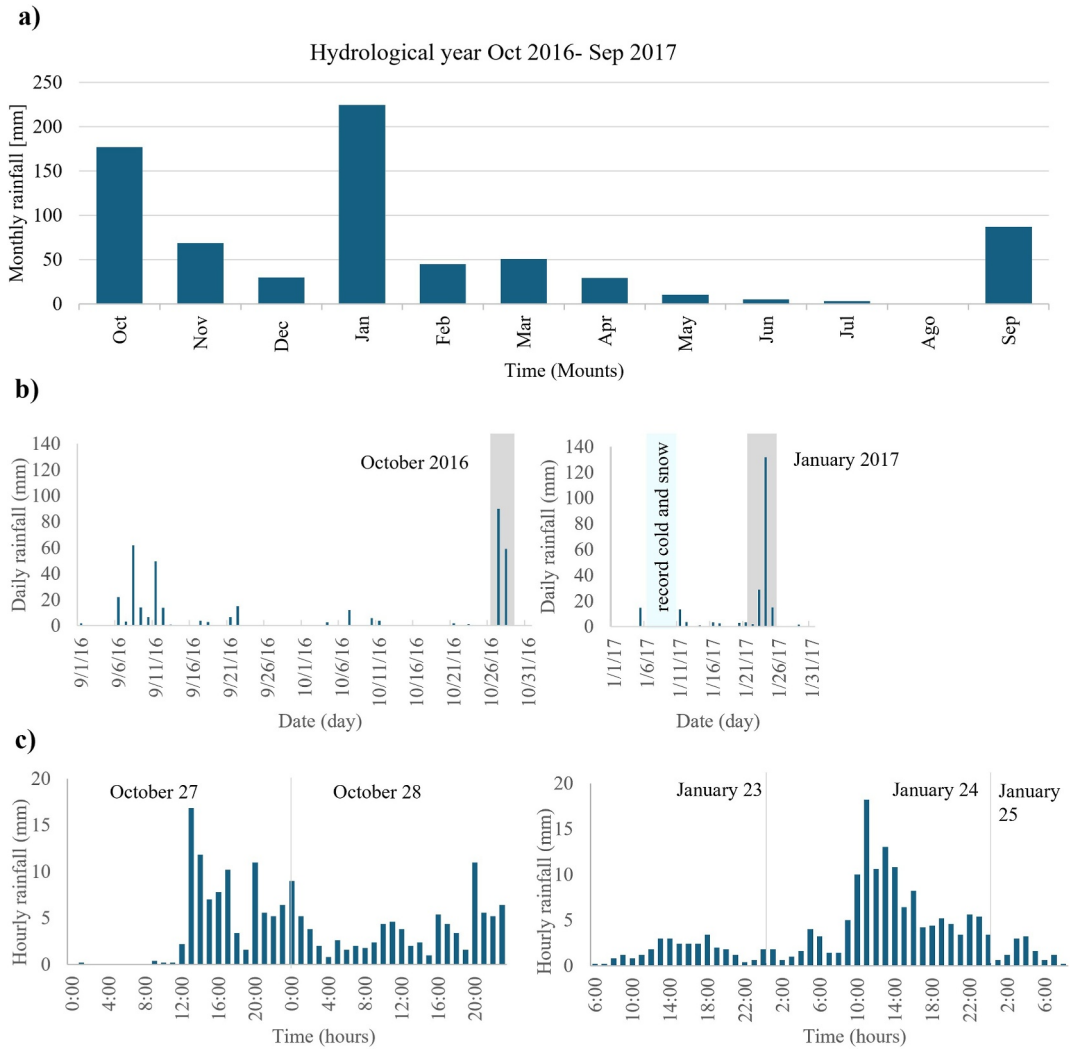

Figure 2. (a) Rainfall data at the Cropalati rain gage for the hydrological year October 2016–September 2017. (b) Daily data for September–October 2016 and January 2017. Areas shaded in gray indicate the rainfall events of October 27–28, 2016, and January 23–25, 2017. The light blue area indicates the record cold event of January 2017. (c) Hourly data recorded on October 27–27, 2016, and January 23–25, 2017.

The selected events have duration of at least 6 hr, exceeding the time of concentration t_c at the Cropalati bridge (C. Viparelli & Viparelli, 1979), and an intensity matching one of the largest measured over one or few years (Bertoldi et al., 2010). The time of concentration is estimated as (Giandotti, 1934)

$$t_c = \frac{4\sqrt{A} + 1.5L}{0.8\sqrt{H_m - H_o}} \tag{1}$$

where A is catchment area (262 km^2), L is river length upstream of the study section (28 km), H_m is average catchment elevation above mean sea level (810.4 m) and H_o is elevation of the study section above mean sea level (136 m) (Versace et al., 1989). We further exclude all events that cannot be isolated over the time interval necessary to acquire 20–30 consecutive SAR images (approximately 5 months if the revising time is 6/8 days) because long rainy periods do not generate a well-defined flood wave.

Figure 2 reports daily and hourly rainfall data measured at the Cropalati rain gage. Two successive isolated events with similar characteristics, duration of approximately two days and 48-hr rainfall depth of approximately 180 mm, are considered in this study. They occurred on October 27–28, 2016, and January 23–25, 2017, and were

respectively associated with moderate and maximum flood warning levels. Average rainfall intensity over a time interval equal to the time of concentration (6 hr) is 9.5 mm/hr in October 2016 and 11.5 mm/hr in January 2017. These values are relatively frequent in the area with a return period smaller than 6–7 years (C. Viparelli & Viparelli, 1979).

Hourly rainfall is presented in the bottom panels of Figure 2c to highlight an important difference between the events. The maximum intensity in October 2016 was recorded at the beginning of the rainfall, while it occurred during the second day of the January 2017 flood. Thus, runoff generated in the 6-hr-long interval with average rainfall intensity equal to 11.5 mm/hr (January) was larger than in October due to higher intensity and because more rainfall was lost due to infiltration in October than in January.

A closer look at the data further highlights differences between the two events. October 2016 was relatively warm (average temperature around 20°C) and the rainfall of October 27–28 happened after 45 predominantly sunny days (left panel of Figure 2b). The January event, on the contrary, was characterized by moderate winds from the South with average temperature around 8°C. It followed the record cold week of January 7 with winds from the Northeast, an average temperature around 0°C and record snowfall (13.2 mm at Cropalati gage). Under these conditions, the rainfall contributed to formation of a flood wave that increased discharge compared to the October 2016 flood. In short, the January 23–25 rainfall closely resembles a rain-on-snow event, so it is expected to generate a flood with significant geomorphic impacts (D. Li et al., 2019).

3. Material and Methods

3.1. Active Width: Instantaneous Versus Morphological

Detailed field campaigns on gravel bed braided rivers indicate that water depth is predominantly shallow with deep areas occupying only 10%–20% of the wetted section over a wide range of discharges (Mosley, 1982, 1983). As discharge increases, flow depth increases in previously wet channels, and new shallow areas form as previously dry channels are inundated. Consequently, depth distribution remains practically unchanged over a wide range of discharges (Mosley, 1982, 1983). The velocity distribution resembles the depth distribution, with high velocity occurring in the deepest part of the wetted section. A significant increase in the fraction of the cross section with high depth and velocity occurs at very high discharges, which on the Ohau River, New Zealand, correspond to the 50-year flood (Mosley, 1982).

The distributions of water depth and velocity described by Mosley (1982, 1983) are key to explain braided river dynamics. They indicate that at a given point in time and over a wide range of discharges, a large portion of the flow (50%–95%) is conveyed in one or few main, active branches where bedload transport occurs (Ashmore, 1991a; Egozi & Ashmore, 2009; Mosley, 1982). Individual branches migrate laterally, exchange water and sediment at bifurcations and confluences, experience cutoffs and avulsions that cause major changes in braided network configuration. As sediment is exchanged between individual branches and with the braidplain, some branches are reactivated, and others become inactive (Ashmore, 2001).

Braided rivers adjust to increasing discharge by increasing wetted width and number of branches while water depth and velocity (i.e., bed shear stress) remain mostly unchanged (Ashmore & Sauks, 2006). Consequently, bedload transport is more sensitive to changes in active width than to changes in depth, which primarily control bedload transport in single-thread rivers (Peirce et al., 2018, 2019). Indeed, if wetted width and depth are used in bedload transport calculations, transport rates are systematically underestimated because the transverse variability of local hydraulics must be accounted for in presence of complex morphologies (Bertoldi, Ashmore, & Tubino, 2009; Francalanci et al., 2012; Paola, 1996; Recking et al., 2016, 2024). Thus, determining active width and number of active branches is fundamental to quantify sediment fluxes and river dynamics in general, as well as to respond to recent regulatory needs to improve river management practices, such as the European Water Framework Directive EC 2000/60 and Flood Directive EC 2007/60 (Ashmore et al., 2011; Rossi et al., 2023).

Active width is typically estimated with two distinct approaches, the instantaneous and the morphological approach. The former is related to quantification of instantaneous bed material flux, and the latter to the quantification of morphological change caused by bed material transport in a specified time interval (Ashmore et al., 2011). Instantaneous active width can be imagined as the width of a cross section where bed material is in transport at a given point in time. Estimating this width may not be straightforward for the difficulty in observing

particle motion but can be done with numerical models using measured cross sections and different flow conditions (Bertoldi, Ashmore, & Tubino, 2009).

Quantitative estimates of morphological active width are obtained by identifying areas of erosion and deposition, that is areas where morphological change occurs, from repeated surveys (Ashmore & Church, 1998). Morphological estimates vary with survey type and frequency, with longer time intervals resulting in smaller morphological sediment fluxes due to compensation mechanisms such as lateral movement of individual channels and bedform migration (Lindsay & Ashmore, 2002). Morphological active width and bedload transport estimates have relied on aerial photos, time-lapse photography, repeated surveys to measure ground movement and, more recently, on the analysis of satellite data (Calle et al., 2020; Carson & Griffith, 1989; Ferguson, 1993; Ferguson et al., 1992).

Survey technique, frequency and spatial resolution vary with river size (e.g., topographic vs. bathymetric surveys), data source (satellite visiting time, frequency of aerial surveys) and time scales of interests. For example, surveys can be repeated with specified frequency because of study needs (Calle et al., 2020; Goff & Ashmore, 1994) or technology constraints such as satellite revisiting time (Crivellaro et al., 2024). In other studies, field data are collected before and after floods (Bertoldi et al., 2010; Misset et al., 2020; Rossi et al., 2023), and publicly available data are used to estimate morphological change over longer time intervals (Lauer et al., 2017; Luchi et al., 2007).

The satellite-based studies mentioned above (Rossi et al., 2023; Smith et al., 1996) used instantaneous measurements of wetted width and braided channel network to estimate discharge and flood dynamics, respectively. In addition, Crivellaro et al. (2024) used instantaneous measurements of wetted width to estimate morphological active widths over seasonal and annual time scales. This approach, however, is inadequate for ephemeral streams, because wetted areas cannot be delineated when the river is not in flood.

The proposed approach is based on the analysis of information on ground movement (DInSAR data) to identify the morphologically active part of a braidplain. It does not rely on the delineation of the wetted area, and this makes it appropriate for applications to ephemeral streams. Noting that in ephemeral streams months long dry periods may separate successive floods, satellite images to perform a statistically meaningful DInSAR analysis may be recorded between one flood and the next. For this reason, the proposed procedure has the potential to provide event-based estimates of active channel width, that is a level of detail typically obtained with field surveys (see e.g. Bertoldi et al., 2010; Ferguson et al., 1992; Goff & Ashmore, 1994).

3.2. The Proposed Methodology: Analysis of DInSAR Data

DInSAR data are analyzed in subsequent steps to estimate morphological change of the braidplain in terms of morphological active width and morphological number of active branches. *Morphological number of active branches* indicates the number of branches that might have been active during the study period. It does not indicate the number of branches that transported bed material at the same point in time, that is the active braiding intensity defined by Egozi and Ashmore (2009), that corresponds to an instantaneous description of the active river.

The proposed methodology consists of data preprocessing (Section 3.3) and a main procedure for image analysis and connectivity-based channel extraction to estimate the morphological number of active branches and active width.

Preprocessing starts with mapping braidplain areas that are covered by vegetation at the end of the study period using optical images. These areas are assumed to represent parts of the braidplain where significant morphological change did not occur (e.g., Bertoldi et al., 2014; Calvani et al., 2019; Stecca et al., 2023). Maps containing vegetated areas and PS locations are integrated to transfer information from the satellite grid to the study area. The area is divided into a regular cartesian grid oriented downvalley and the total number of PSs inside a circular buffer distance from the cell centroid is assigned to each grid cell.

The Stability Index (SI) is the PS count of each cell for a given buffer size divided by the maximum number of PSs detected with that buffer size in the study area. SI ranges from 0 to 1 and allows us to compare results obtained with buffers differing in size. Morphological change is unlikely to occur in areas with many PSs (SI near 1), while change is possible where no or few PSs are present (SI near 0). Vegetated areas are assumed to be very stable and

assigned a value of SI = 1. It is important to note that the proposed interpretation of SI maps is based on the assumption that morphological change, and thus bedload transport, did not occur in some unvegetated parts of the braidplain, so that the highest spatial density of PSs (SI near 1) is representative of areas that remained inactive in the study period. The proposed method should not be adequate for applications when the entire braidplain is reworked, for example in relatively narrow braidplains or in case of very large floods.

Stability Index (SI) maps identify areas where morphological changes may have occurred, but they require further interpretation to estimate the morphological number of active channels and the active channel width. This is achieved by transforming the continuous SI variable (range 0–1) into binary maps via the Stability Threshold (ST). Cells with SI values lower than ST are classified as *potentially active* (SI < ST, SI = 1), whereas those with values higher than ST are considered *inactive* (SI > ST, SI = 0). In the analysis presented below, ST ranges between a minimum value below which the entire study area is considered inactive, and a maximum value corresponding to the condition above which the entire area is classified as potentially active. Several binary SI-ST maps are created by co-varying buffer size and ST threshold value.

The binary maps are input to a connectivity algorithm to identify spatially continuous paths of potentially active cells linking the upstream and downstream ends of the study area. In other words, when potentially active cells are spatially connected across an entire specified reach, they are part of a spatially continuous path. If the connected path does not cross the entire reach, the *potentially active* cells cannot be classified as active.

A simple algorithm to identify spatially continuous paths of potentially active cells is illustrated herein. It was developed to manually identify spatially continuous paths following specific rules depending on: (a) the minimum number of adjacent cells to define a channel, (b) the maximum number of consecutive rows that can be skipped before re-identifying the next cluster of adjacent cells, and (c) the degree of overlap between two successive rows of active cells needed for the path to be considered valid. This algorithm will be replaced by more efficient and robust computational approaches in future applications.

The network of spatially continuous paths of active cells obtained from the connectivity algorithm is used to estimate the morphological number of active branches and the morphological active width for different combination of SI map (buffer radius) and ST values. Cross-sections showing the transverse variability of SI are extracted from the SI maps. Spatially continuous paths of active cells where SI ≤ ST are considered morphologically active branches. The morphological active width is defined as the sum of the widths of cross section areas surrounding active branches with SI ≤ ST. A continuous path of potentially active cells surrounded by inactive cells are considered inactive for that combination of SI map and ST.

These calculations provide different estimates of morphological active width and number of active channels in the same study period for all SI-ST combinations. Minimum, maximum and average values are compared to determine the variability of estimated morphological active width and number of active channels around the mean. This is illustrated and discussed with the application to the Trionto River in Section 4.

3.3. Available Data and Preprocessing

Optical images of the study site are used to identify the braidplain areas that are covered by vegetation, considered parts where without morphological change. Differential Interferometry of Synthetic Aperture Radar data (DInSAR) (Gabriel et al., 1989) is conducted on Sentinel-1 SAR images with a resolution of 20 m × 4 m and 6 days of revisiting time. As 20–30 images are required, the duration of data collection is of several (4–6) months. Images are selected to estimate morphological change caused by each flood, as well as the combined effect of the two events.

Satellite data are processed using SUBSIDENCE v.28, software based on Coherent Pixels Technique (CPT) to measure ground deformation (Mora et al., 2003), which is based on the principle of Multitemporal Interferometry SAR (MT-InSAR) using stacks of images covering large periods. CPT involves the following processing steps:

- *Data selection*: SAR images must be acquired in interferometric configuration, that is with specified incidence angles and orbits (Mora et al., 2003). In particular, CPT uses Single Look Complex (SLC) data that includes phase information of the received signal.
- *Coregistration*: SLC images must have the same sampling grid to perform multi-temporal analysis of ground displacement. Coregistration is therefore necessary to align acquisitions so that the same point on the ground

corresponds to the same pixel in all images of the interferometric stack. It is important to note that coregistration does not introduce errors that can propagate in the analysis, as the image registration occurs one time to align all images with a reference image.

- *Generation of interferograms and coherence maps*: Coregistered images are compared with a master image to generate interferograms representing the phase difference between individual acquisitions and the master image. Interferograms are analyzed with coherence maps. Interferometric coherence is an index of target stability that is particularly relevant for this application because in case of gravel braidplains only areas with high coherence values can be considered reliable for ground displacement estimation.
- *Pixel selection to identify PSs*: A Permanent Scatterers (PS) represents an element that has a relatively constant electromagnetic response. PS coherence varies between 0 and 1, with 1 representing perfect stability over time (no movement), and 0 lack of coherence. The lack of coherence indicates large target movement, presence of a poorly reflective surface such as water, or movable targets such as vegetation leaves.
- *Generation of maps and time series of displacement* is required to study temporal evolution of ground deformation. In particular, differential interferograms (comparison of successive acquisitions) are used to quantify ground movement.
- *Geocoding* is the final step to project ground movement from the radar reference system to the projected reference system WGS84-UTM.

The last two steps are performed to measure displacement. Recalling that we are using DInSAR to identify areas of the braidplain where displacement cannot be measured, the last two steps of the typical DInSAR analysis are unnecessary for the procedure presented below.

4. Application to the Trionto River

Rainfall data at the Cropalati gage reported in Figure 2 indicates that the only periods of possible morphological change in the 2017 hydrologic year (from October 2016 to September 2017) were the October 2016 and January 2017 floods. In particular, we identified the following study periods: 22 September 2016–22 January 2017 (21 images; prior to January 2017 flood) to isolate the October 2016 flood; 3 November 2016–30 August 2017 (51 images) to isolate the January 2017 flood, and 16 October 2016–29 September 2017 (56 images) including both floods. Start and end dates of the study periods differ (e.g., the first and the third intervals could have started on the same day) because we refined the analysis as research progressed. It is important to recall that exact start and end dates of the study periods are not relevant, as long as a sufficient number of images collected in a time interval including the storm events in question is available.

4.1. Identification of Active Cells

Maps containing vegetated areas and PSs location are illustrated in Figure 3a, where PSs of the October 2016-September 2017 period are represented with green dots and vegetated areas with solid light brown. Vegetated areas of Figure 3 are from a December 2017 image downloaded from Google Earth and used as background of most figures of the paper. DInSAR data at the Trionto River study site are composed of 18,000 PSs with coherence values no less than 0.75 for the 16 October 2016–29 September 2017 period; 25,000 of such PSs for the October 2016 event (22 September 2016–22 January 2017) and 20,000 PSs with coherence greater than 0.75 for January 2017 event (3 November 2016–30 August 2017). The larger number of PSs suggests less braidplain movement in October 2016 than in January 2017.

DInSAR results are transferred from the 20 m × 4 m satellite grid to a 4 m × 4 m local grid oriented downvalley (Figure 3a). A coarser local grid would have caused loss of relevant information because data pertaining to more than one satellite grid cell would have been averaged. Conversely, a finer local grid would have increased computational costs without adding useful information to the analysis.

Figure 3a illustrates circular buffers used to evaluate the number of PSs to each grid cell. As shown in the inset of Figure 3a, larger buffers likely contain more PSs on average than smaller ones and the probability of not finding PSs in a buffer increases as buffer radius decreases. Five values of buffer size (8, 10, 12, 14, and 16 m) are used to generate SI maps (Figures 3b and 3c). The values range is selected considering that a buffer equal to the cell size (4 m) would have provided redundant information. Starting with a buffer radius equal to 8 m (twice the cell size) ensures that additional spatial information is integrated, while preserving local variability. Buffers larger than 16 m excessively reduce the level of detail.

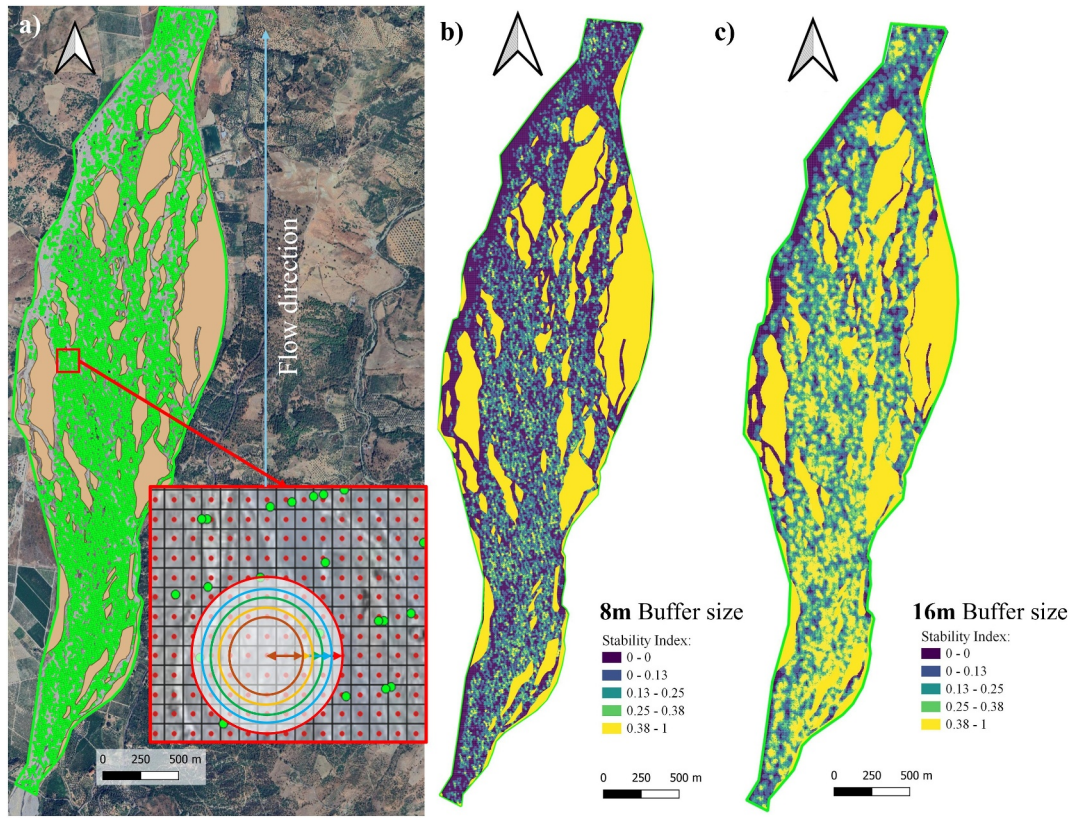

Figure 3. (a) Map with permanent scatterers (PSs) in green, vegetated areas in December 2017 in solid light brown. The inset illustrates how information on the spatial density of PSs is transferred from the satellite grid to the local grid. (b) Map showing stability index (SI) index for the 8 m buffer radius. (c) Map showing SI index for the 16 m buffer radius. Data pertains to the October 2016–September 2017 period.

Panels b and c of Figure 3 illustrate SI maps obtained with 8 and 16 m buffers. In the figure, the color scale indicates likely mobile parts in violet (SI < 0.13), vegetated and likely immobile areas in yellow (SI > 0.38) and areas with intermediate SI value in green. Maps with large buffer radius present a less pronounced spatial variability of SI than maps obtained with a small buffer radius because they average over a larger area, so the local variability of PS patches is smoothed out of the SI data (Figure 3a).

Stability Thresholds ST equal to 0.05, 0.1, 0.15 and 0.2 are used to binarize the SI maps. A threshold lower than 0.05 would show a grid composed of almost all inactive cells, on the contrary a threshold greater than 0.20 would show a grid composed of almost all active cells obtaining little significant information. Active cells of the binary maps are represented in Figure 4 for buffer radius equal to 12 m and ST equal to 0.05 and 0.2 (Figures 4a and 4b) and for buffer radii equal to 8 and 16 m and ST = 0.15 (Figures 4c and 4d). Figure 4 illustrates how the number of active cells increases for increasing ST values for a fixed buffer radius (panels a and b) and decreases with buffer size for a fixed ST value (panels c and d). A connected path of active cells is visible in hydraulic left (yellow box) for all combinations of buffer radius and ST suggesting that the left part of the braidplain might have been morphologically active. Binary maps obtained for all combinations of buffer radius and ST for the three study periods are reported in Figures S1–S3 in Supporting Information S1.

The average number of active cells per row is computed over 45 rows (all combinations are shown in Figures S4 in Supporting Information S1), corresponding to a downstream distance of approximately 200 m (Figure 5a), to identify the binary maps with similar downstream distribution of active cells for different buffer radii (Figure 5b). These maps are presented in Figure 5, where the streamwise change of average number of active cells in the boxes (a) and (b) are present in the panels.

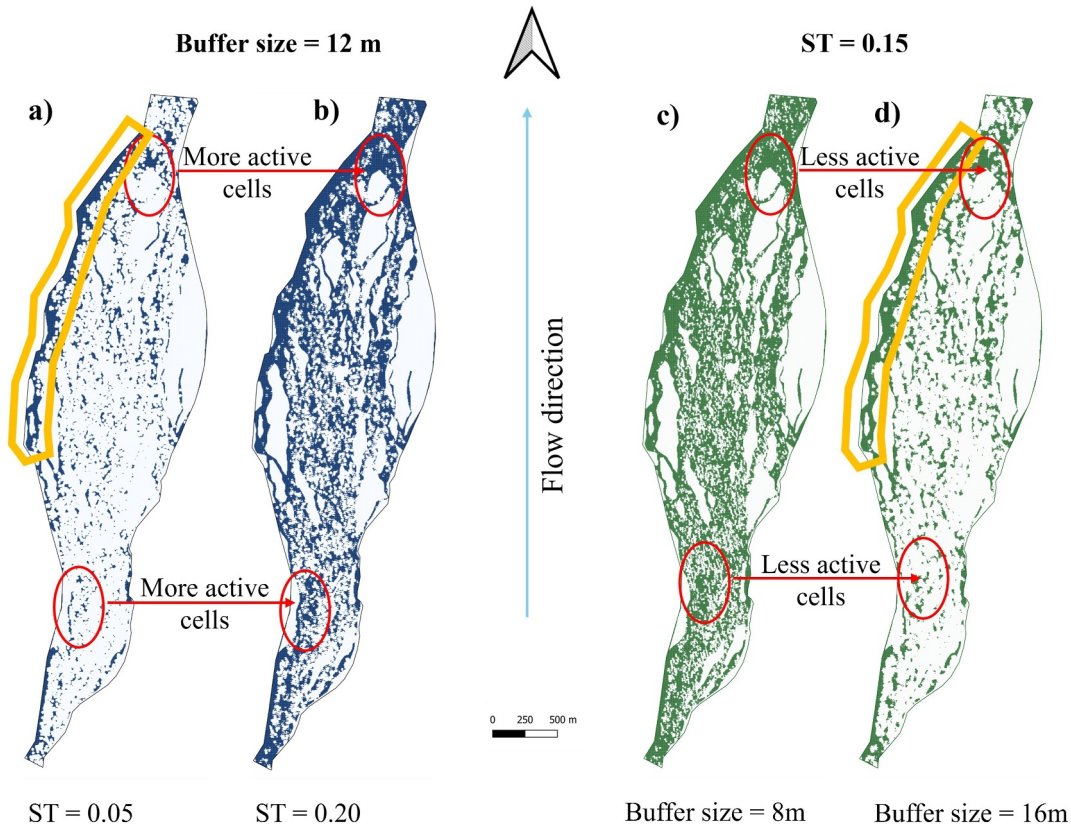

Figure 4. Areas of potentially active cells identified for different combination of buffer radius and stability threshold (ST) values. Blue and green denote cells with stability index smaller than the ST (potentially active). The yellow box highlighted the presence of an area of connected potentially active cells close to the left bank. Data pertains to the October 2016–September 2017 study period. (a) Buffer radius equal to 12 m ST equal to 0.05; (b) Buffer radius equal to 12 m, ST equal to 0.20. (c) Buffer radius equal 8 m, ST equal to 0.15; (d) Buffer radius equal to 16 m, ST equal to 0.15.

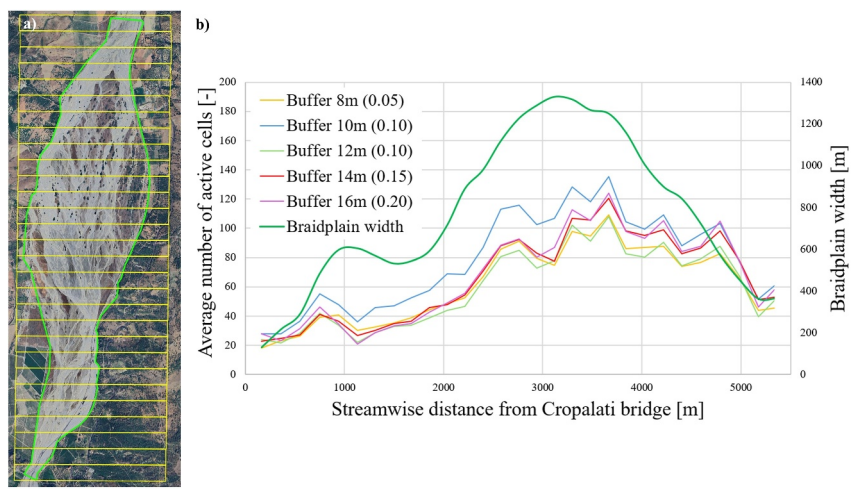

Figure 5. Combination of buffer radius and stability threshold (ST) resulting in similar average number of potentially active cells per row. (a) Division of the study area in 29 strips composed of 45 rows of the local grid. (b) Variability of the average number of potentially active cells for five combinations of buffer radius and ST values providing similar results. All combinations are shown in Figures S4 in Supporting Information S1. The green line indicates braidplain width.

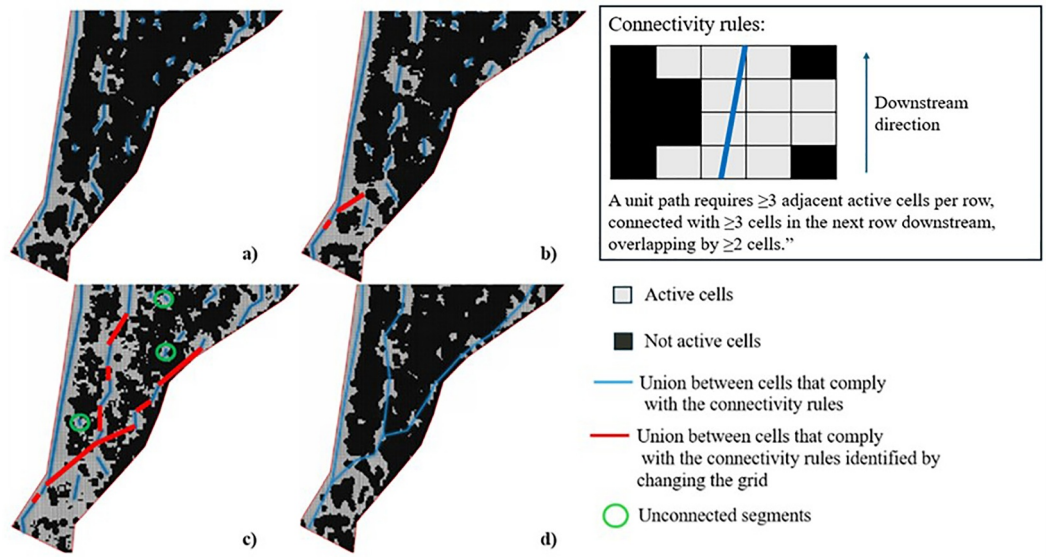

Figure 6. Connectivity algorithm for the identification of spatially continuous paths of potentially active cells in the upstream part of the study area. (a) identification of path elements from the maps of Figure 5. (b) identification of new path elements using buffer radius equal to 12 m and ST equal to 0.10. (c) elements that are not part of a spatially continuous path are deleted (the binary matrix at the base is the one corresponding to the Buffer 10 m ST = 0.10 combination). (d) The network of continuous paths overlaid on the matrices in panel (a).

To identify spatially continuous paths of active cells, the binary maps of Figure 5 are overlaid, as shown in Figure 6a for the upstream part of the study area, where common active cells (value = 0) to all five matrices are indicated in gray.

The connectivity algorithm considers unit paths defined by three or more neighboring active cells in a row (≥12 m) that are adjacent to three or more active cells in the next downstream row with an overlap of at least two cells, as illustrated in the top-right panel of Figure 6. In Figure 6a, spatially continuous segments composed of connected unit paths, that is unit paths with an overlap between rows of at least two cells, are represented with blue lines. The result is a fragmented network of unconnected segments. Additional binary maps are used to connect these segments (see Figures S1–S3 in Supporting Information S1). In Figure 6b, a binary map with a buffer radius of 12 m and ST = 0.10 is superimposed to the map of Figure 6a: red lines show new connections between previously fragmented segments. The process is repeated with other binary maps until one or more spatially continuous paths connect the upstream and downstream sections of the study site. Segments that remain unconnected are identified (green circles in Figure 6c) and subsequently removed. The final network of spatially continuous paths is shown in Figure 6d. Lower buffer radius values (8 m) and ST values (0.05) did not provide additional connectivity information. Networks for the three study periods are presented in Figure 7, where the red dot represents the Cropalati bridge.

The study reach is further divided into five, 1 km long portions progressively numbered downstream with relatively uniform braidplain width and slope. In addition, cross sections are drawn 250 m apart (thin lines in Figures 7a –7c) to compare estimated morphological change qualitatively and quantitatively. Networks of spatially continuous paths of potentially active cells of the January 2017 flood (panel b) and the October 2016–January 2017 period (panel c) are practically the same in the upstream, narrow part of the study area (portions 1 and 2). Three continuous paths are identified downstream of the Cropalati bridge, two paths are close to the left bank and one to the right bank. The continuous path by the right bank is absent in the network of the October 2016 flood (panel a). Differences between networks are most evident in the widest part of the braidplain (portions 3 and 4). The October 2016 channel network (Figure 7a) has the smallest number of spatially continuous paths with one path in the center of the braidplain in portion 3 and all paths close to the left bank further downstream. The January 2017 channel network is noticeably more complex in the widest part of the braidplain with paths intersecting one another and occupying both the left and right parts of the braidplain. Finally, the network of Figure 7c extracted

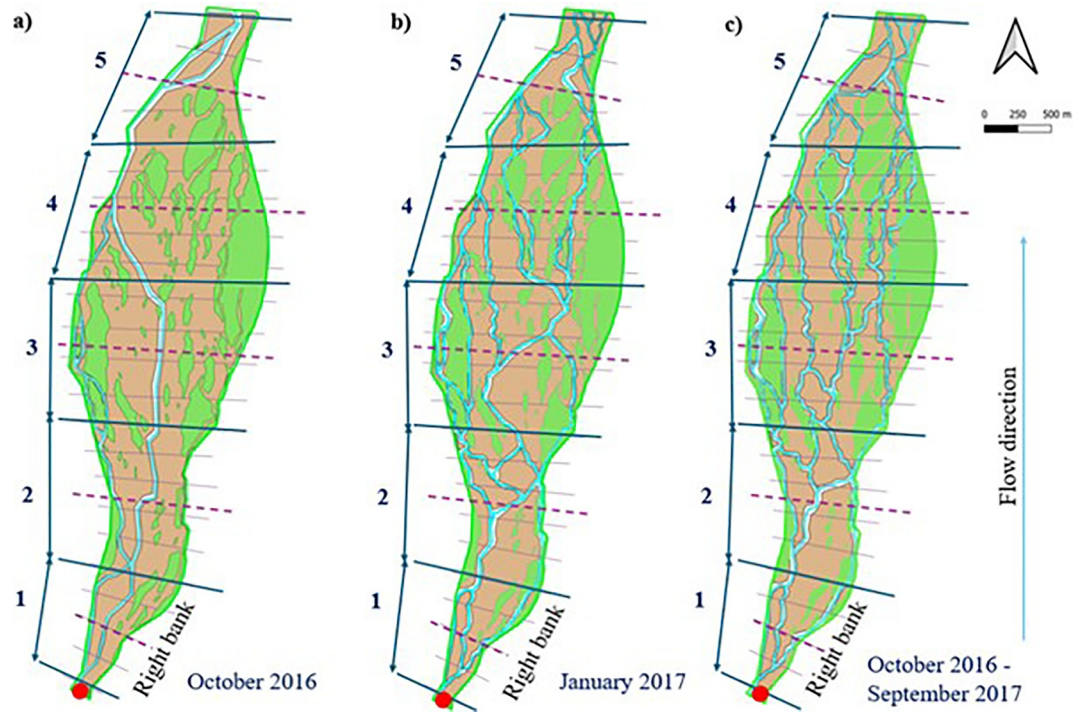

Figure 7. Network of spatially continuous paths of potentially active cells for (a) October 2016 event (b) January 2017 event and (c) Sum of both events October 2016 plus January 2017. Red dots indicate the Cropalati bridge. Thin gray segments are cross sections where the number of continuous paths is computed. Thick blue lines denote 1 km long sections of the study area where indexes of Table 1 are computed, and dash purple lines at the midpoint of each section.

from October 2016–September 2017 data covering both events is even more intricate than the network of Figure 7b particularly where the braidplain is widest (portions 3 and 4).

4.2. Estimates of Morphological Active Width and Number of Active Branches

The steps to estimate morphological active width and number of active branches for all combinations of buffer radius (SI map) and ST are illustrated in Figure 8 for the October 2016–September 2017 period and buffer radius equal to 12 m. These steps are repeated for all buffer radii and all study periods. The objective is to determine, for each study period, the variability of different estimates around a local average value, and how this local average changes downstream during a study period and from one study period to the other.

The network of spatially continuous paths of potentially active cells (Figure 8a) is superimposed to the SI map (Figure 8b) to identify possible locations of active branches in the 23 cross sections spaced of approximately 250 m downvalley (thin lines in Figures 8a and 8b). Red lines in Figure 8 indicate cross Sections 4, 15 and 22 represented in Figures 8c–8e, where continuous blue lines show the transverse variability of SI. Red dots mark the intersection points between the spatially continuous paths (Figure 8a) and each cross section.

The continuous paths falling within areas with SI $\leq$ ST are considered morphologically active for that combination of buffer radius and ST. This is illustrated in Figures 8c–8e, for the same ST values used to generate the binary maps of Figure 4 and Figures S1–S3 in Supporting Information S1 (i.e., ST = 0.05, 0.10, 0.15 and 0.20). In general, the analysis can be done for any value of ST that is reasonable for a specific application. Pink lines in Figure 8 identify parts of the cross section surrounding continuous paths (red dots) with SI $\leq$ 0.05. The active width estimate for this buffer radius ST combination is equal to the total length of the pink segments. Similarly, green, light blue and orange lines identify the cross section surrounding continuous paths with SI $\leq$ 0.10, SI $\leq$ 0.15 and SI $\leq$ 0.20 respectively.

Interestingly, in the narrow upstream part of the study reach, Section 4 and Figure 8c, the morphological active part of the cross section is located close to the left bank for all ST values. In other words, the continuous path close

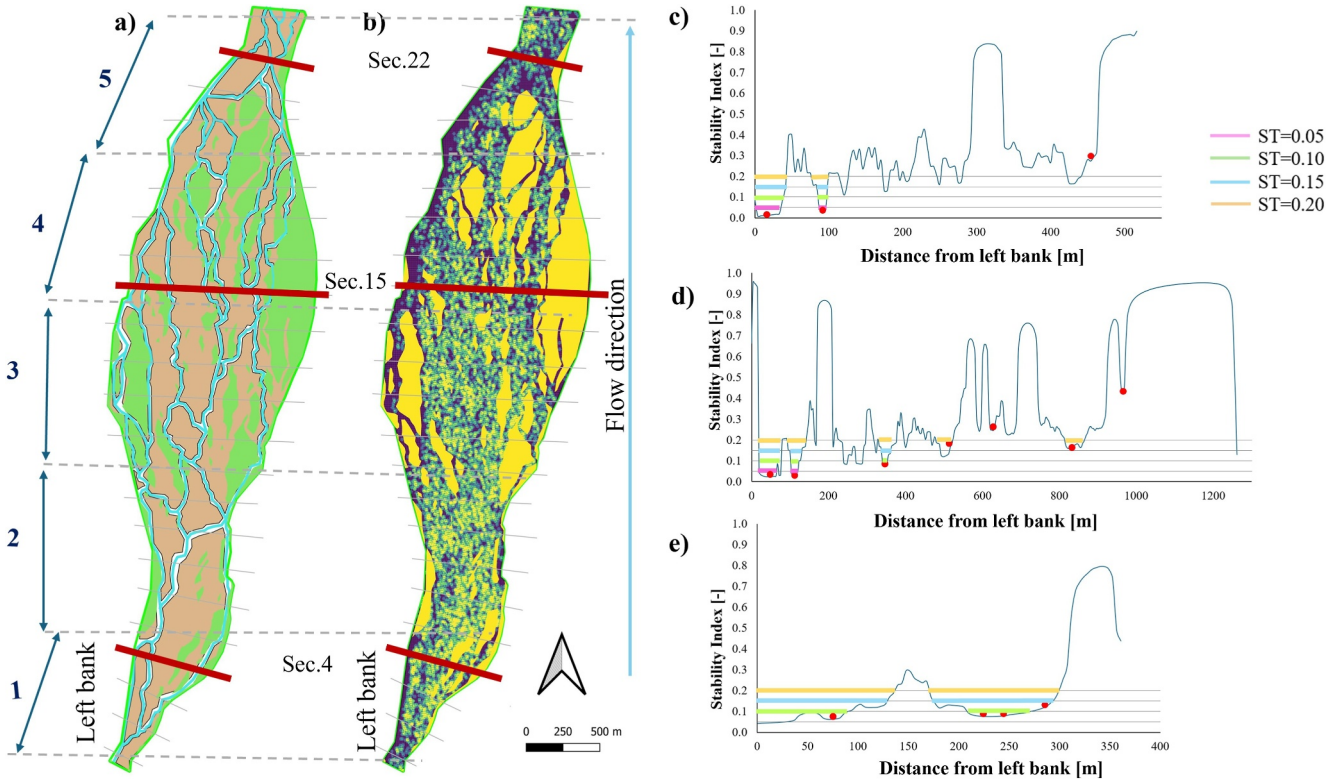

Figure 8. (a) Study area with networks of spatially continuous paths of potentially active cells for the October 2016–September 2017 period. Gray lines indicate 23 cross sections at approximately 250 m apart. The red lines are cross sections 4, 15 and 22. (b) network of panel (a) superimposed to the stability index map obtained using buffer radius equal to 12 m. (c–e) estimate of the number of active channels (red dots) and of the active width in cross ections 4 (c), 15 (d) and 22 (e).

to the right bank is not considered active for a buffer radius is equal to 12 m. In this cross section and for buffer radius equal to 12 m, active width only moderately increases with ST.

The analysis at cross section 15, which is in the widest part of the braidplain, is not as straightforward. As ST increases from 0.05 to 0.2, the number of morphological active branches increases from two to five. For ST = 0.15 (light blue lines) three morphologically active branches are located close to the left bank. When ST increases to 0.2 (yellow lines), two more spatially continuous paths are classified as active. One of these paths is in the central part of the cross section and the other is close to the vegetated island by the right bank. Consequently, in this cross section active width estimates noticeably increase when ST varies from 0.15 to 0.2. It is important to note that two continuous paths at distance of approximately 600 and 1,000 m from the left bank remain inactive for all ST values.

In the downstream part of the study reach (Figure 8e) there is no morphological active path for buffer size equal to 12 m and ST = 0.05, as indicated by the absence of pink lines. For ST > 0.05, two active areas are separated by relatively high SI values at approximately 150 m from the left bank. The area close to the left bank contains one active continuous path. The area on the right contains at least two spatially continuous paths. These paths, however, are not separated by zones with SI > ST and for this reason, number of estimated active branches is equal to two.

Figure 9 illustrates how the spatial distribution of morphologically active branches varies with ST values for the October 2016 (panels a and b) and January 2017 (panels c and d) floods using a buffer value equal to 12 m. The analysis is conducted in the same cross sections of Figure 8. Light blue lines in Figure 9 represent the network of spatially continuous paths of potentially active cells (Figures 7a and 7b), black dots identify active branches in each cross section, dashed black lines connect black dots that are found on the same continuous path and in successive cross sections downstream. As ST increases, the number of active branches per cross section increases and more paths are classified as active. For the October 2016 event (panel a and panel b) the presence of active

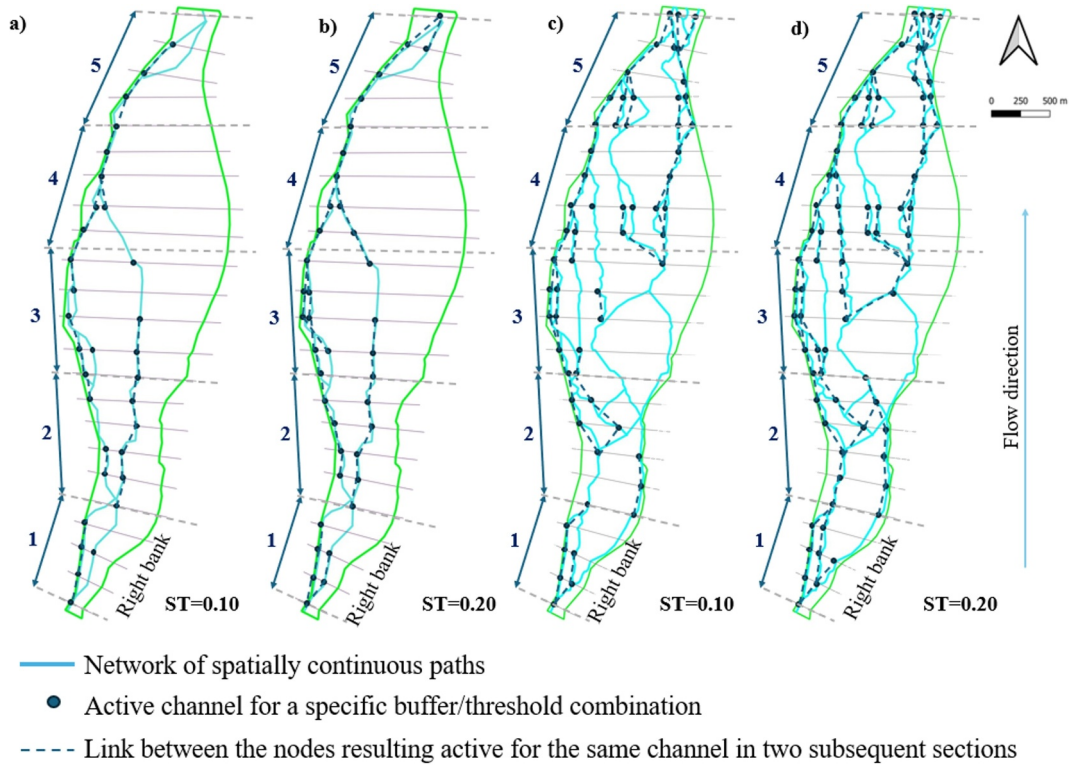

Figure 9. Comparison between the network of spatially continuous paths of potentially active cells and the networks obtained for different buffer and threshold combination (black dots and dashed lines). (a) October 2016 event with 12 m buffer and ST = 0.10. (b) October 2016 event with 12 m buffer and ST = 0.20. (c) January 2017 event with 12 m buffer and ST = 0.10. (d) January 2017 event with 12m buffer and ST = 0.20.

channels is evident close to the left bank and in the center of the riverbed for ST = 0.1 and 0.2. For the January 2017 event (panel c and panel d), at ST = 0.1 active branches are primarily predicted close to the left bank. As ST increases to 0.2, the procedure identifies morphologically active branches also close to the right bank in portions 1 and 2 and in the central part of the wide portions 3 and 4.

Figure 10 shows how the estimated number of morphologically active branches varies downstream for the three study periods. Results are presented in terms of minimum and maximum (gray line marker) and average (yellow triangle) number of branches. Black dots indicate values estimated with and all combinations of buffer radius and ST. For the October 2016 flood, up to two morphologically active branches are predicted everywhere in the braidplain. The estimated number of morphologically active branches in the upstream narrow portions 1 and 2 of the braidplain for the January 2017 flood is larger than for October 2016 because morphological change is also estimated close to the right bank (Figures 7 and 10). Estimated morphological change for the January 2017 flood is also larger than for the October 2016 flood in the wide part of the braidplain (portions 3 and 4) with up to five morphologically active branches estimated.

The average number of active branches estimated for the October 2016–September 2017 period is similar to that of the January 2017 flood in the narrow upstream part of the braidplain (portions 1 and 2), but it is highest in the wide part of the braidplain (portions 3 and 4) suggesting that the two floods may have reworked different parts of the braidplain where the braidplain is widest.

Similar results are presented in Figure 11 in terms of estimated morphological active width (pink, green, light blue and yellow lines in Figure 8) equal, on average, to 50 m for the October 2016 flood everywhere at the study site. In the narrow upstream part of the braidplain (portions 1 and 2) average morphological active width for the January 2017 flood and the October 2016–September 2017 period remains equal to 50 m. Data, however, indicate larger variability around the average value for the January 2017 flood than for the October 2016 flood due to the

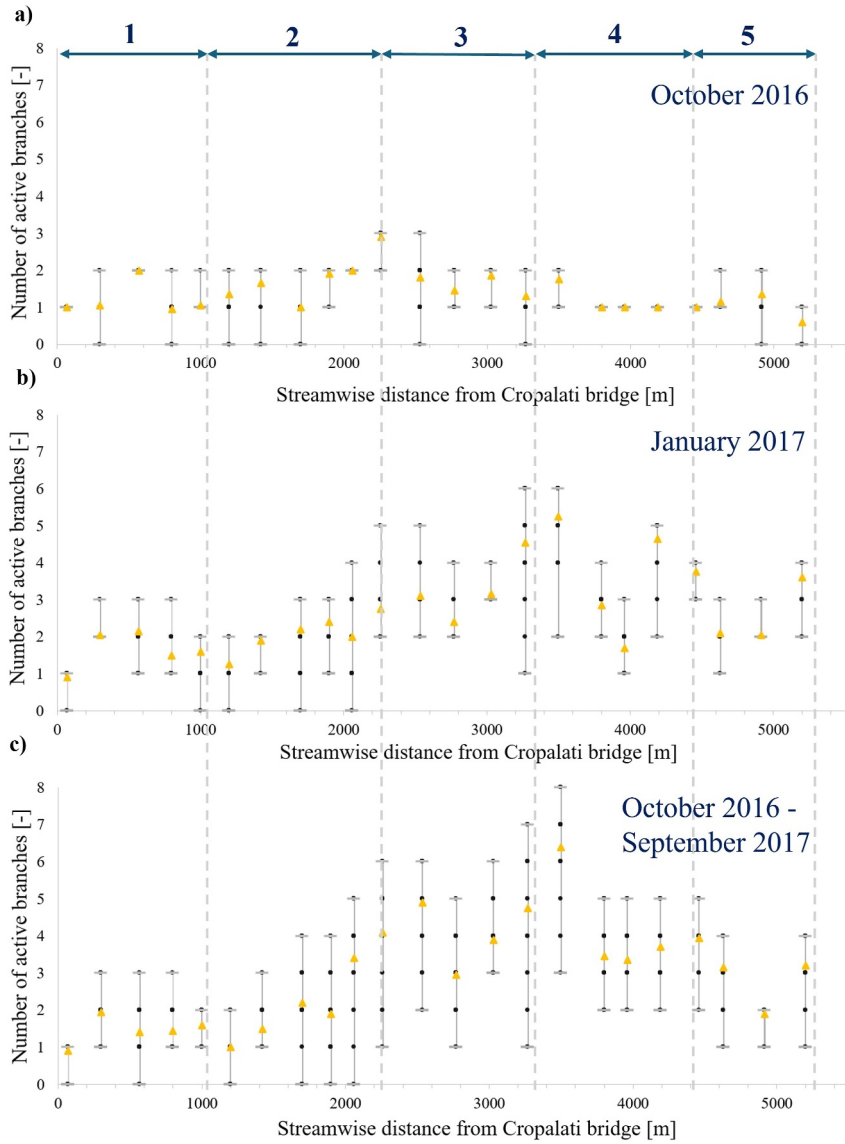

Figure 10. Number of active branches for different combinations of buffer radius and stability threshold values: minimum, maximum (gray lines) and average (yellow triangle) number of active channels for (a) October 2016 flood, (b) January 2017 flood, (c) September 2016–October 2017 period.

presence of an active branch close to the right bank. Active width estimates in this narrow braidplain, however, rarely exceed 100 m.

In the wide part of the braidplain (portions 3 and 4), as well as in the narrow convergent portion 5, the morphological active width estimated for the January 2017 flood is much larger (150 m on average) than that of the October 2016 flood indicating widespread morphological change. The narrow section approximately 4 km downstream of the Cropalati bridge is due to the presence of vegetated islands that increase the lateral confinement of the flow.

Estimates of morphological active width for the October 2016–September 2017 period in portions 3–5 of the braidplain show lager variability around the average value (150 m) than those of the January 2017 flood further suggesting that the October 2016 and the January 2017 floods might have reworked two somewhat distinct parts of the braidplain.

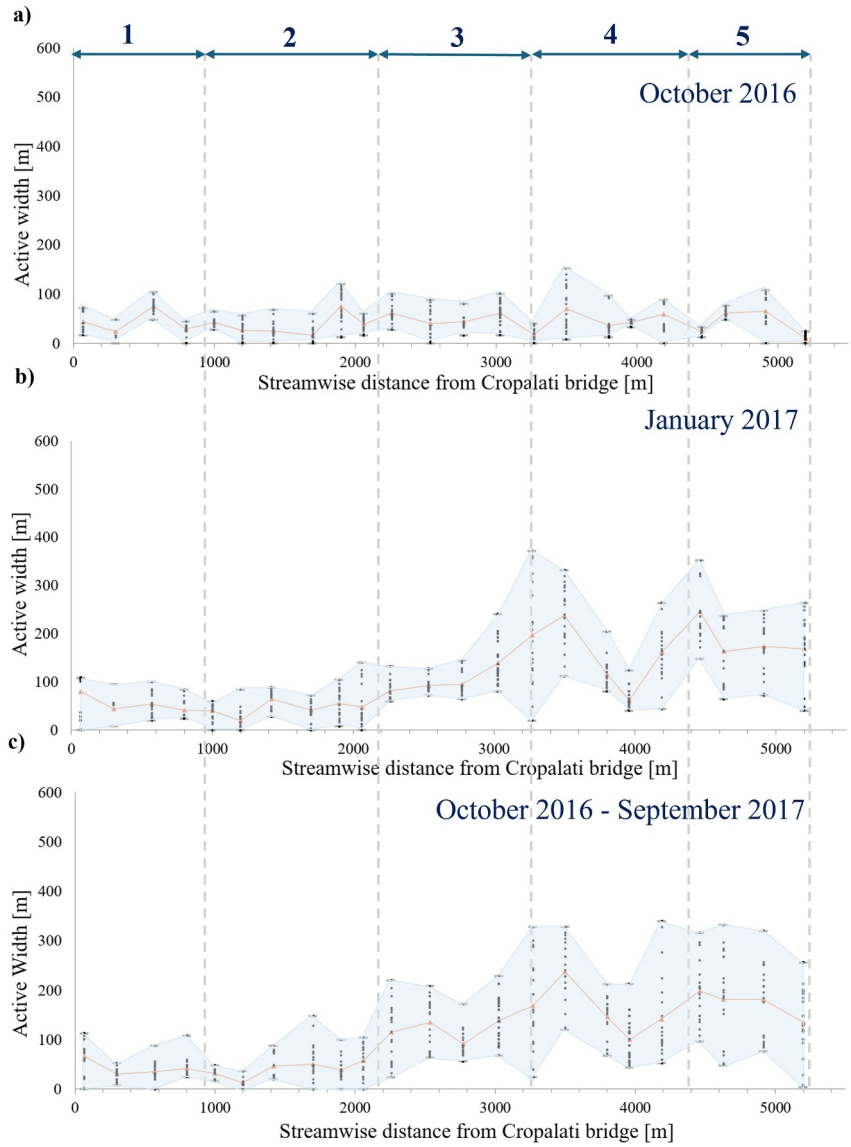

Figure 11. Active width estimates for different combinations of buffer radius and stability threshold value. B_B (braidplain width) is listed in picture. The orange line denotes the average value. (a) October 2016 event, (b) January 2017 event, (c) October 2016–September 2017 period.

5. Discussion

The estimate of morphological change from DInSAR data on the Trionto River indicates that the proposed approach has the potential to capture features of braided rivers that have been documented with laboratory experiments and field data.

Estimated average morphological active width remains spatially unchanged for the relatively small flood of October 2016 (Figure 11a) while it increases in the wide part of the braidplain for the larger January 2017 event (Figure 11b) suggesting that the method proposed herein can capture the increase of morphological active width and active braided intensity with flow discharge (Ashmore et al., 2011; Peirce et al., 2019).

Morphological change during the October 2016 flood is estimated close to the left bank and in the upstream central part of the cross section with one or two channels being active in the upstream portions 1–3 and one channel being active close the left bank in portions 3–5 (Figures 9a and 9b). The morphological active width does

not vary downstream indicating that changes in braidplain width have very little influence on sediment transport processes for this flood event.

The number of active branches and active width estimated in the upstream narrow portions 1 and 2 are similar for both flood events (Figures 10 and 11), where only one to three active branches form with an average active width on the order of 50 m. In the wide portions of the braidplain, however, the estimated morphological number of active branches and active width are considerably larger after the larger flood (January 2017), indicating that the flow reworked a wide portion of the braidplain. The increase in active braided intensity (number of active channels at a given point in time) and active width with flow discharge has been documented in laboratory experiments with model braided rivers (Egozi & Ashmore, 2009; Peirce et al., 2018, 2019). Further, the increased complexity of braided rivers with increased braidplain width has also been shown in laboratory experiments specifically designed to study the effect of lateral confinement on braided river morphodynamics (Carbonari et al., 2020; Garcia Lugo et al., 2015).

The different morphological response of a braided river to different types of floods has been documented in Alpine, gravel bed braided rivers (Bertoldi et al., 2010; Misset et al., 2020). In particular, Bertoldi et al. (2010) note that flow and flood pulses generate different morphological change in the perennial Tagliamento River, Italy. Flow pulses are small frequent floods that cause morphological change in just one or two branches and in a limited portion of the braidplain. Flood pulses, conversely, are less frequent and cause change in network geometry with more than two channels being active during the event. The morphological change estimated with our procedure suggests that the smaller October 2016 flood caused morphological change in a limited portion of the braidplain and could thus be considered a flow pulse. The larger January 2017 flood, on the contrary, caused widespread morphological change and network reorganization (up to 5 active branches during the event) and can thus be considered a flood pulse.

5.1. Comparison With Optical and Multispectral Images

Landsat images downloaded from Google Earth and a SPOT7 satellite 6 m resolution multispectral image are used to further investigate if the proposed procedure may have captured the different response of the Trionto River to flow and flood pulses. This comparison represents a qualitative attempt to evaluate the results of the analysis presented above. Landsat images were taken in June 2015 (Figure 12a) and July 2017 (Figure 12e) and the multispectral image is dated 13 April 2017 (Figure 12d). The June 2015 image was collected at low flow and a wetted channel is visible in the central, upstream part of the braidplain and is indicated with the red oval in Figure 12a. The location of this channel roughly corresponds to the location of the spatially continuous path of active cells located in the central part of the braidplain for the October 2016 flood (Figure 12b).

Rainfall data at the Cropalati gage indicate that five rainfall events that might have generated morphological change occurred between June 2015 and October 2016. These events, however, had average smaller rainfall intensity over a 6-hr time interval (i.e. the time of concentration at the Cropalati bridge) than the October 2016 rainfall. Noting that unusually wet periods were not recorded between June 2015 and October 2016, these events likely resulted in flow pulses that caused localized change but did not alter braided network geometry.

The Normalized Difference Vegetation Index (NDVI) (Rousse et al., 1973) is used to identify wetted areas in the SPOT7 image. The NDVI is computed in each pixel using red (RED) and near-infrared (NIR) bands as follows:

$$\mathrm{NDVI} = \frac{\mathrm{NIR} - \mathrm{RED}}{\mathrm{NIR} + \mathrm{RED}} \tag{2}$$

NDVI ranges between −1 and 1 and is used to classify different parts of an image. Pixels with NDVI between −1 and 0 are primarily occupied by water. NDVI values just above zero indicate rocks, values above 0.2 correspond to vegetation (Huang et al., 2021). This is indicated in Figure 12d, where green indicates vegetation, yellow and orange gravel (i.e., unvegetated braidplain) and dark orange/red water on 13 April 2017.

The comparison between the images of Figure 12 indicates a clear change in network geometry between October 2016 and April 2017 with the formation of a bifurcation right downstream of the Cropalati bridge. Two channels conveyed water in April 2017, one close to the left bank and the other close to the right bank in the upstream portions 1–3 of the braidplain. The location of the active branches in Figure 12c and of the path corresponding to

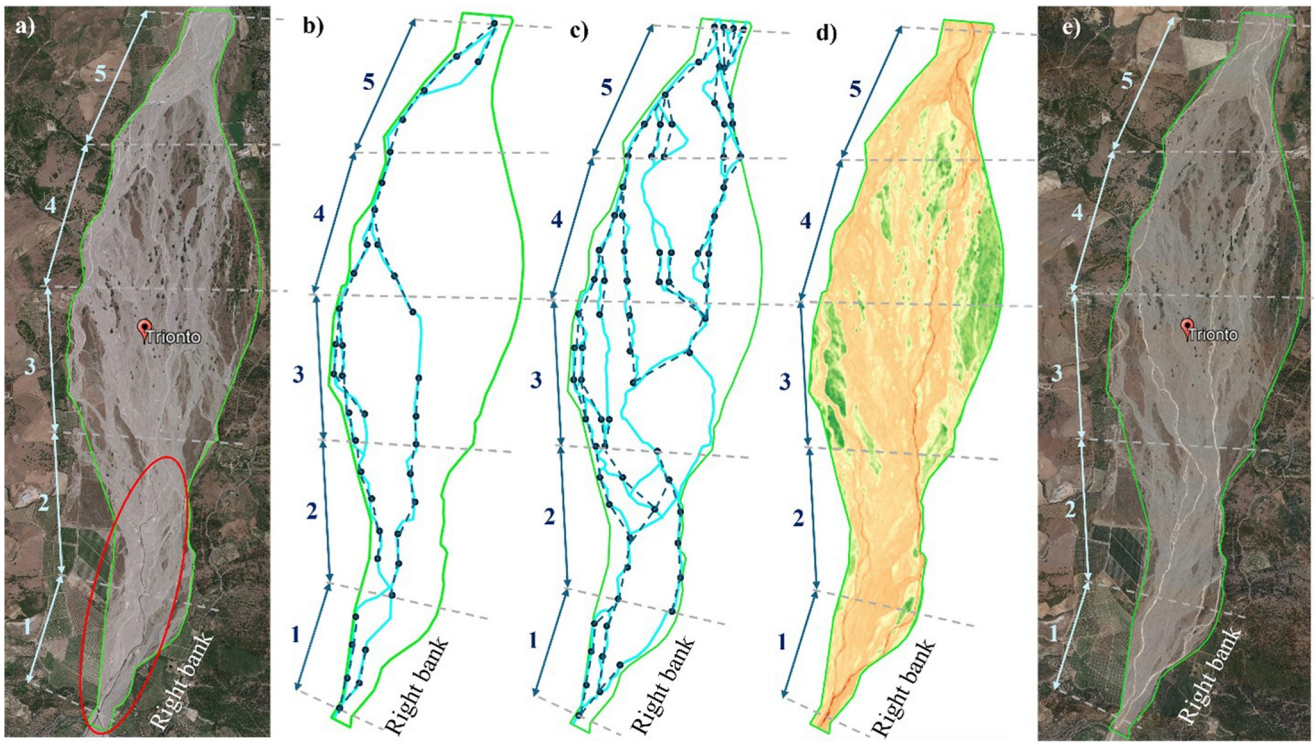

Figure 12. (a) Google Earth image of the study area captured in June 2015. (b) Potentially active and active branches (blue and dashed lines respectively) obtained for October 2016 flood with a 12 m buffer radius and stability threshold (ST) equal to 0.20. (c) Potentially active and active branches obtained for January 2017 flood with a 12 m buffer radius and ST equal to 0.20. (d) NDVI map for the SPOT7 satellite 6 m resolution image dated 13 April 2017. (e) Google Earth image of the study area captured in July 2017.

water of NDVI image (Figure 12d) are similar to the location of channels highlighted in Figure 12e, suggesting that the discharge at low flow was conveyed by branches that were active during the January 2017 flood. In the central and downstream portions 3–5 of the braidplain, the flow in July 2017 was conveyed in a channel close to the left bank and in another channel in the central-right part of the braidplain between vegetated islands. These channels are in areas of the braidplain where morphological change is estimated in for the January 2017 flood, and where the NDVI image of Figure 12d suggests presence of water.

The comparison between the April 2017 multispectral image (Figure 12d) and the Landsat image dated July 2017 (Figure 12e) suggests minimum change of the braided network. Rainfall data at the Cropalati gage for this time interval indicate that three rainfall events that might have caused morphological change had 6-hr rainfall intensity smaller than the October 2016 rainfall, and unusually wet periods were not recorded. Thus, these events likely generated flow pulses and did not cause a major reorganization of the braided network, in agreement with the insight of the proposed procedure to estimate morphological change in braided, gravel bed rivers.

5.2. Quantification of Network Complexity

Different indices and parameters have been defined to quantify and synthetically describe the complexity of braided channel networks (Egozi & Ashmore, 2008). For example, braiding intensity synthetically describes the complexity of the network of wetted or active branches over a relatively long distance downstream. Bar indices based on bar and island dimensions are used to quantify spatial distribution of confluences and bifurcations. Channel counts are another measure of network complexity, and sinuosity provides information on how channelized a braidplain is (Egozi & Ashmore, 2008; Howard et al., 1970). Cross section averaged parameters describing at-a-station or downstream hydraulic geometry such as width, depth and number of branches are also defined for both wetted and the active sections of braided rivers (e.g., Ashmore et al., 2011).

The networks of Figure 7 are compared using indices that resemble those that describe braided river networks. The number of paths per cross section (every 250 m) is presented in Figure 13 and is analogous to the number of

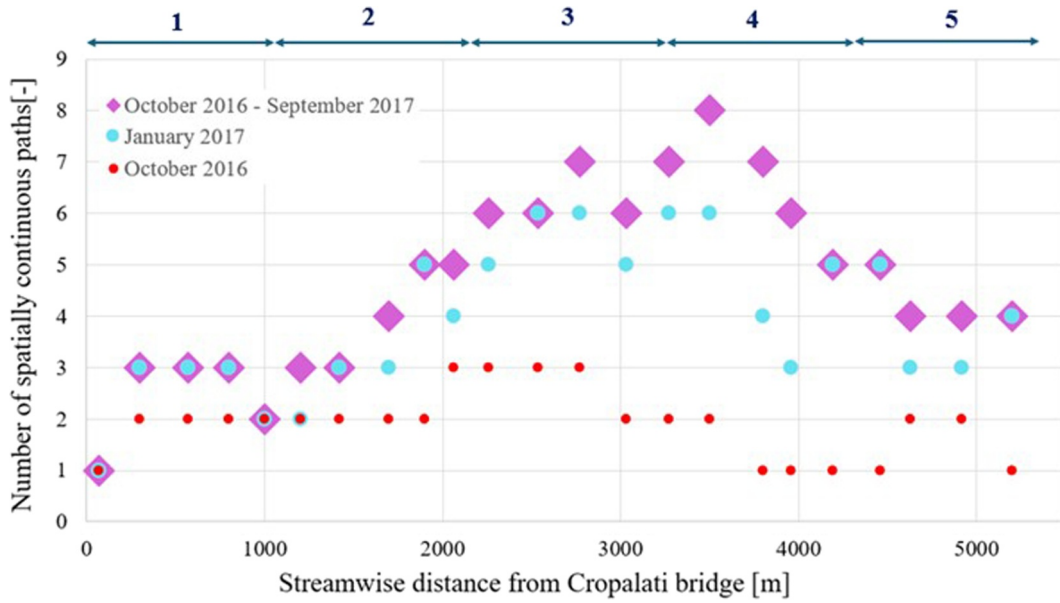

Figure 13. Streamwise variation of the number of spatially continuous paths of active channels in the 23 cross sections starting from Cropalati bridge. Purple diamonds represent the results considering both events (October 2016 plus January 2017), light blue dots represent the result for January 2017 event and red dots represent the result for October 2016 event.

active channels per cross section proposed by Egozi and Ashmore (2008). Red and light blue dots in Figure 13 are respectively representative of the networks of Figures 7a and 7b (October 2016 and January 2017 floods), pink diamonds describe the network of Figure 7c (October 2016–September 2017). The number of spatially continuous paths is always largest where the braidplain is widest (portions 3 and 4). The number of paths extracted for the October 2016 flood is smaller than that of the January 2017 flood and the largest number of paths is extracted for the October 2016-January 2017 period including both floods.

Total sinuosity S, excess segment index E and number of channels per kilometer N (Egozi & Ashmore, 2008; Howard et al., 1970) are used to describe network complexity over the one-kilometer-long portions of the braidplain of Figure 7. Total sinuosity S is defined as total path length per unit downvalley distance in each portion of the braidplain, E is the average number of paths bisected by cross sections at the boundaries and in the center of each portion of the braidplain (blue and purple lines of Figure 7, respectively), and N is total number of paths entering and entirely contained within each portion of the braidplain (Howard et al., 1970).

Table 1
Complexity of Networks of Spatially Continuous Paths of Potentially Active Cells in Terms of Total Sinuosity S, Excess Segment Index E and Number of Channels per Kilometer N

			October 2016			January 2017			October 2016–January 2017		
Portion	Slope (−)	B_B (m)	S	E	N	S	E	N	S	E	N
1	0.007	360 m	1.84	1.67	1	2.56	2	4	2.56	2	4
2	0.010	720 m	2.31	2.33	2	4.07	3	10	4.21	3	8
3	0.015	1,140 m	2.79	2.67	6	5.78	5	10	7.2	6	17
4	0.011	1,100 m	1.61	1.67	2	5.93	5	12	8.82	6.33	26
5	0.015	610 m	1.96	1.33	3	4.72	4	11	4.95	4.33	15

Note. Braidplain slope and width B_B are also reported for the five portions of the study site.

Downvalley changes in braided indices are summarized in Table 1. The table also reports slope and average width B_B of each portion of the braidplain. Slope at the study site is highest in the widest sections, in agreement with results of laboratory experiments showing higher sediment transport capacities in narrow braidplains for the same flow discharge and braidplain slope (Garcia Lugo et al., 2015; Warburton, 1996). In agreement with the results of Figure 13, all braided indices increase with valley width reinforcing the finding that the analysis reasonably indicates the presence of a more complex network in the widest part of the braidplain (Ashmore, 2013; Carbonari et al., 2020; Garcia Lugo et al., 2015).

Indices describing morphological change caused by two floods (October 2016–September 2017) are the largest. Further, indices pertaining to the January 2017 flood are larger than those describing the network of the October 2016 flood, providing additional evidence that most morphological change occurred during the largest flood, in agreement with results of laboratory experiments and field observations (e.g., Ashmore, 2001; Egozi & Ashmore, 2009; Hundey & Ashmore, 2009; Peirce et al., 2019; Ragno et al., 2022; Robertson-Rintoul & Richards, 1993).

Table 2
Complexity of Morphologically Active Networks for Buffer Size Equal to 12 m and Different ST Values in Terms of Total Sinuosity S and Excess Segment Index E

			ST = 0.05		ST = 0.10		ST = 0.15		ST = 0.20	
Portion	Slope (−)	B_B (m)	*S*	*E*	*S*	*E*	*S*	*E*	*S*	*E*
(a) October 2016 Buffer 12 m										
1	0.007	360 m	0.50	0.67	0.75	0.67	0.75	0.67	0.75	0.67
2	0.010	720 m	0.40	0.67	1.60	1.33	1.60	1.33	1.60	1.33
3	0.015	1,140 m	0.78	1.00	1.33	1.00	1.56	1.67	1.56	1.67
4	0.011	1100 m	0.78	1.00	1.33	1.33	1.56	1.67	1.56	1.67
5	0.015	610 m	0.75	0.67	0.75	0.67	1.00	1.00	1.00	1.00
(b) January 2017 Buffer 12 m										
1	0.007	360 m	1.00	0.67	1.50	1.67	1.75	2.00	2.50	2.00
2	0.010	720 m	1.00	1.00	1.30	2.00	2.40	2.33	2.30	2.33
3	0.015	1,140 m	1.78	2.00	1.89	2.67	2.22	2.33	3.22	3.33
4	0.011	1,100 m	1.56	3.00	2.89	3.33	4.22	3.33	4.22	4.33
5	0.015	610 m	3.50	3.33	3.75	3.33	4.25	3.67	1.25	3.67

Note. Braidplain slope and width B_B are also reported for reference.

A quantitative comparison between the networks of Figure 9 and the network of spatially continuous paths (Figure 7) is presented in Table 2 in terms of total sinuosity *S* and excess segment index *E*. The values of *S* and *E*, as expected, grow as the threshold increases, remaining below the values characterizing the continuous paths of active cells (Table 1). Further, *S* and *E* are smallest for the October 2016 flood, which is expected to have caused the least morphological change, and they only modestly increase with braidplain width. Estimates of *S* and *E* for the active network of the January 2017 flood show are larger in portions 3 and 4 than in the upstream part of the study site and, interestingly, remain large in the relatively narrow confluence zone (portion 5) downstream, suggesting that more complex network of branches might have been active in the downstream part of the study site, where upstream influence likely plays a prime morphological control.

6. Conclusions

Notwithstanding recent research efforts to understand braided river dynamics, estimating the active geometry of braided, gravel bed rivers remains challenging due to the rapidly evolving geometry during floods and to the coexistence of multiple spatial scales (Paola, 2001). Building on recent advances in remote sensing technology, we propose a methodology to estimate morphological change of a braidplain from Differential Interferometry of Synthetic Aperture Radar data (DInSAR). Strength of the proposed approach is the absence of algorithms to distinguish between wet and dry areas of the braidplain, which makes it appropriate for applications to ephemeral streams.

The methodology is applied to identify morphological change on a 5 km long reach of the ephemeral Trionto River caused by two floods. The application demonstrates that the proposed approach has the potential to predict morphological change that varies with river confinement and discharge magnitude in agreement with results of laboratory experiments and field observations (e.g., Ashmore, 2013; Ashmore et al., 2011; Bertoldi et al., 2010; Garcia Lugo et al., 2015; Peirce et al., 2018, 2019).

The comparison between estimates of morphological change integrated with rainfall information, optical and high-resolution multispectral images indicates that the procedure can reasonably detect the position of channels in the braidplain, as well as the different morphological response of a braided river to different types of floods. In particular, the estimated response of the Trionto River to relatively small and frequent floods (flow pulses) consist of localized change around one or two active branches. In response to relatively large and rare floods (flood pulses), the morphological change is widespread with changes in braided network geometry. It is important to note that the comparison with Google and satellite images (Figure 12) represents only a qualitative comparison

with field data and does not constitute a complete validation of the methodology. Systematic validation will be carried out through dedicated field measurements starting in the fall of 2025. The procedure will also be tested on other rivers to fully assess its reliability, general applicability and extension to perennial systems.

Conflict of Interest

The authors declare no conflicts of interest relevant to this study.

Data Availability Statement

The data sets for this research are available in following citation: Guadagno (2025) and can be accessed through the following URL: https://doi.org/10.17632/pxv3tvfzr7.1.

Acknowledgments
Support of a INPS (Italian National Institute of Social Security) doctoral fellowship to the first author and of the NSF award CBET 1751926 is acknowledged. The authors sincerely thank Michal Tal for her comments on an earlier version of the manuscript and three anonymous reviewers for feedback that greatly helped improve the manuscript, and the editor for the careful handling of the submission and constructive suggestions.

References

Ashmore, P. (1991a). Channel morphology and bedload pulses in braided, gravel-bed streams. *Geografiska Annaler - Series A: Physical Geography*, *73*(1), 37–52. https://doi.org/10.1080/04353676.1991.11880331

Ashmore, P. (1991b). How do gravel bed rivers braid? *Canadian Journal of Earth Sciences*, *28*(3), 326–341. https://doi.org/10.1139/e91-030

Ashmore, P. (2001). Braiding phenomena: Statics and kinetics. In M. P. Mosley (Ed.), *Gravel-Bed Rivers V*. Water Resources Publications, LLC.

Ashmore, P. (2013). Morphology and dynamic of braided rivers. In E. Whol (Ed.), *Chapter 17, Treatise on geomorphology 9: Fluvial geomorphology* (pp. 289–317).

Ashmore, P., Bertoldi, W., & Gardner, J. T. (2011). Active width of gravel-bed braided rivers. *Earth Surface Processes and Landforms*, *36*(11), 1510–1521. https://doi.org/10.1002/esp.2182

Ashmore, P., & Church, M. (1998). Sediment transport and river morphology: Paradigm for study. In P. C. Klingeman, R. L. Beschta, P. D. Komar, & J. B. Bradley (Eds.), *Chapter 7 Gravel-bed rivers in the environment*. Water Resources Publications, LLC.

Ashmore, P., & Sauks, E. (2006). Prediction of discharge from water surface width in a braided river with implications for at-a-station hydraulic geometry. *Water Resources Research*, *42*(3), W03406. https://doi.org/10.1029/2005wr003993

Bertoldi, W., Ashmore, P., & Tubino, M. (2009). A method for estimating the mean bed load flux in braided rivers. *Geomorphology*, *103*(3), 330–340. https://doi.org/10.1016/j.geomorph.2008.06.014

Bertoldi, W., Siviglia, A., Tettamanti, S., Toffolon, M., Vetsch, D., & Francalanci, S. (2014). Modeling vegetation controls on fluvial morphological trajectories. *Geophysical Research Letters*, *41*(20), 7167–7175. https://doi.org/10.1002/2014gl061666

Bertoldi, W., Zanoni, L., & Tubino, M. (2009). Planform dynamics of braided streams. *Earth Surface Processes and Landforms*, *34*(4), 547–557. https://doi.org/10.1002/esp.1755

Bertoldi, W., Zanoni, L., & Tubino, M. (2010). Assessment of morphological changes induced by flow and flood pulses in a gravel bed braided river: The Tagliamento River (Italy). *Geomorphology*, *114*(3), 348–360. https://doi.org/10.1016/j.geomorph.2009.07.017

Calle, M., Calle, J., Alho, P., & Benito, G. (2020). Inferring sediment transfers and functional connectivity of rivers from repeat topographic surveys. *Earth Surface Processes and Landforms*, *45*(3), 681–693. https://doi.org/10.1002/esp.4765

Calvani, G., Francalanci, S., & Solari, L. (2019). A physical model for the uprooting of flexible vegetation on river bars. *Journal of Geophysical Research: Earth Surface*, *124*(4), 1018–1034. https://doi.org/10.1029/2018jf004747

Carbonari, C., Recking, A., & Solari, L. (2020). Morphology, bedload, and sorting process variability in response to lateral confinement: Results from physical models of gravel bed rivers. *Journal of Geophysical Research: Earth Surface*, *125*(12), e2020JF005773. https://doi.org/10.1029/2020JF005773

Carson, M. A., & Griffiths, G. (1989). Gravel transport in the braided Waimakariri River: Mechanisms, measurements and predictions. *Journal of Hydrology*, *109*(3–4), 201–220. https://doi.org/10.1016/0022-1694(89)90016-4

Cohen, H., & Laronne, J. B. (2005). High rates of sediment transport by flashfloods in the southern Judean Desert, Israel. *Hydrological Processes*, *19*(8), 1687–1702. https://doi.org/10.1002/hyp.5630

Colesanti, C., Ferretti, A., Prati, C., & Rocca, F. (2003). Monitoring landslides and tectonic motions with the permanent scatterers technique. *Engineering Geology*, *68*(1–2), 3–14. https://doi.org/10.1016/S0013-7952(02)00195-3

Colesanti, C., & Wasowski, J. (2006). Investigating landslides with space-borne Synthetic Aperture Radar (SAR) interferometry. *Engineering Geology*, *88*(3–4), 173–199. https://doi.org/10.1016/j.enggeo.2006.09.013

Conesa-Garcia, C., Puig-Mengual, C., Riquelme, A., Tomas, R., Martinez-Capel, F., Garcia-Lorenzo, R., et al. (2022). Changes in stream power and morphological adjustments at the event-scale and high spatial resolution along an ephemeral gravel-bed channel. *Geomorphology*, *398*, 108053. https://doi.org/10.1016/j.geomorph.2021.108053

Crivellaro, M., Vitti, A., Zolezzi, G., & Bertoldi, W. (2024). Characterization of active riverbed spatiotemporal dynamics through the definition of a framework for remote sensing procedures. *Remote Sensing*, *16*(1), 184. https://doi.org/10.3390/rs16010184

Czapiga, M. J., McElroy, B., & Parker, G. (2019). Bankfull shields number versus slope and grain size. *Journal of Hydraulic Research*, *57*(6), 760–769. https://doi.org/10.1080/00221686.2018.1534287

Dunne, K. B. J., & Jerolmack, D. J. (2018). Evidence of, and proposed explanation for, bimodal transport states in alluvial rivers. *Earth Surface Dynamics*, *6*(3), 583–594. https://doi.org/10.5194/esurf-6-583-2018

Dunne, K. B. J., & Jerolmack, D. J. (2020). What sets river width? *Science Advances*, *6*(41), eabc1505. https://doi.org/10.1126/sciadv.abc1505

Egozi, R., & Ashmore, P. (2008). Defining and measuring braiding intensity. *Earth Surface Processes and Landforms*, *33*(14), 2121–2138. https://doi.org/10.1002/esp.1658

Egozi, R., & Ashmore, P. (2009). Experimental analysis of braided channel pattern response to increased discharge. *Journal of Geophysical Research*, *114*(F2), F02012. https://doi.org/10.1029/2008jf001099

Ferguson, R. I. (1993). Understanding braiding processes in gravel-bed rivers: Progress and unresolved problems. In J. L. Best & C. S. Bristow (Eds.), *Braided Rivers* (Vol. 75, pp. 73–87). Geological Society Special Publication.

Ferguson, R. I., Ashmore, P. E., Ashworth, P. J., Paola, C., & Prestegaard, K. L. (1992). Measurements in a braided river chute and lobe 1. Flow pattern, sediment transport and channel change. *Water Resources Research*, *28*(7), 1877–1886. https://doi.org/10.1029/92wr00700

Ferretti, A., Prati, C., & Rocca, F. (2000). Nonlinear subsidence rate estimation using permanent scatterers in differential SAR interferometry. *IEEE Transactions on Geoscience and Remote Sensing*, *38*(5), 2202–2212. https://doi.org/10.1109/36.868878

Ferretti, A., Prati, C., & Rocca, F. (2001). Permanent scatterers in SAR interferometry. *IEEE Transactions on Geoscience and Remote Sensing*, *39*(1), 8–20. https://doi.org/10.1109/36.898661

Francalanci, S., Solari, L., Toffolon, M., & Parker, G. (2012). Do alternate bars affect sediment transport and flow resistance in gravel-bed rivers? *Earth Surface Processes and Landforms*, *37*(8), 866–875. https://doi.org/10.1002/esp.3217

Franceschetti, G., Migliaccio, M., Riccio, D., & Schirinzi, G. (1992). SARAS: A synthetic aperture radar (SAR) raw signal simulator. *IEEE Transactions on Geoscience and Remote Sensing*, *30*(1), 110–123. https://doi.org/10.1109/36.124221

Gabriel, A. K., Goldstein, R. M., & Zebker, H. A. (1989). Mapping small elevation changes over large areas: Differential radar interferometry. *Journal of Geophysical Research*, *94*(B7), 9183–9191. https://doi.org/10.1029/JB094iB07p09183

Garcia Lugo, G. A., Bertoldi, W., Henshaw, A. J., & Gurnell, A. M. (2015). The effect of lateral confinement on gravel bed river morphology. *Water Resources Research*, *51*(9), 7145–7158. https://doi.org/10.1002/2015WR017081

García-Martínez, B., & Rinaldi, M. (2022). Changes in meander geometry over the last 250 years along the lower Guadaldquivir River (southern Spain) in response to hydrological and human factors. *Geomorphology*, *410*, 108284. https://doi.org/10.1016/j.geomorph.2022.108284

Giandotti, M. (1934). Previsione delle piene e delle magre dei corsi d'acqua. In *Memorie e Studi Idrografici* (No. 8).

Goff, J., & Ashmore, P. (1994). Gravel transport and morphological change in braided Sunwapta River, Alberta, Canada. *Earth Surface Processes and Landforms*, *19*(3), 195–212. https://doi.org/10.1002/esp.3290190302

Guadagno, V. (2025). Detecting morphological change from DInSAR data in ephemeral, braided, gravel bed rivers. Application to the ungauged Trionto River, Italy. *Mendeley Data, V1*. https://doi.org/10.17632/pxv3tvfzr7.1

Hassan, M. (1990). Scour, fill, and burial depth of coarse material in gravel bed streams. *Earth Surface Processes and Landforms*, *15*(4), 341–356. https://doi.org/10.1002/esp.3290150405

Hassan, M. (2005). Characteristics of gravel bars in ephemeral streams. *Journal of Sedimentary Research*, *75*(1), 29–42. https://doi.org/10.2110/jsr.2005.004

Hassan, M., Egozi, R., & Parker, G. (2006). Experiments on the effect of hydrograph characteristics on vertical grain sorting in Gravel Bed Rivers. *Water Resources Research*, *42*(9), W09408. https://doi.org/10.1029/2005wr004707

Hassan, M., Marren, P. M., & Schwartz, U. (2009). Bar structure in an arid ephemeral stream. *Sedimentary Geology*, *221*(1–4), 57–70. https://doi.org/10.1016/j.sedgeo.2009.07.012

Howard, A., Keetch, M. E., & Vincent, C. L. (1970). Topological and geometrical properties of braided streams. *Water Resources Research*, *6*(6), 1674–1687. https://doi.org/10.1029/wr006i006p01674

Huang, S., Tang, L., Hupy, J. P., Wang, Y., & Shao, G. (2021). A commentary review on the use of normalized difference vegetation index (NDVI) in the era of popular remote sensing. *Journal of Forestry Research*, *32*, 1–6. https://doi.org/10.1007/s11676-020-01155-1

Hundey, E. J., & Ashmore, P. (2009). Length scale of braided river morphology. *Water Resources Research*, *45*(8), W08409. https://doi.org/10.1029/2008wr007521

Laronne, J. B., & Reid, I. (1993). Very high rates of bedload sediment transport by ephemeral desert rivers. *Nature*, *366*(6451), 148–150. https://doi.org/10.1038/366148a0

Laronne, J. B., Reid, I., Yitshak, Y., & Frostick, L. E. (1994). The non-layering of gravel streambeds under ephemeral flood regimes. *Journal of Hydrology*, *159*(1–4), 353–363. https://doi.org/10.1016/0022-1694(94)90266-6

Lauer, J. W., Echterling, C., Lenhart, C., Belmont, P., & Rausch, R. (2017). Air-photo based change in channel width in the Minnesota River basin: Modes of adjustment and implications for sediment budget. *Geomorphology*, *297*, 170–184. https://doi.org/10.1016/j.geomorph.2017.09.005

Leopold, L. B., & Maddock, T. (1953). *The hydraulic geometry of stream channels and some physiographic implications, Geological survey professional paper 252*. United States Government Printing Office.

Li, C., Czapiga, M. J., Eke, E. C., Viparelli, E., & Parker, G. (2015). Variable shields number model for river bankfull geometry: Bankfull shear velocity is viscosity-dependent but grain size-independent. *Journal of Hydraulic Research*, *53*(1), 36–48. https://doi.org/10.1080/00221686.2014.939113

Li, D., Lettenmaier, D. P., Margulis, S. A., & Andreadis, K. (2019). The role of rain-on-snow in flooding over the conterminous United States. *Water Resources Research*, *55*(11), 8492–8513. https://doi.org/10.1029/2019WR024950

Lindsay, J. B., & Ashmore, P. (2002). The effects of survey frequency on estimated of scour and fill in a braided river model. *Earth Surface Processes and Landforms*, *27*(1), 27–43. https://doi.org/10.1002/esp.282

Luchi, R., Bertoldi, W., Zolezzi, G., & Tubino, M. (2007). Monitoring and predicting channel change in a free-evolving, small Alpine river: Ridanna Creek (North East Italy). *Earth Surface Processes and Landforms*, *32*(14), 2104–2119. https://doi.org/10.1002/esp.1511

Misset, C., Recking, A., Legout, C., Bakker, M., Bodereau, N., Borgniet, L., et al. (2020). Combining multi-physical measurements to quantify bedload transport and morphodynamics interactions in an Alpine braiding river reach. *Geomorphology*, *351*, 106877. https://doi.org/10.1016/j.geomorph.2019.106877

Mora, O., Mallorqui, J. J., & Broquetas, A. (2003). Linear and nonlinear terrain deformation maps from a reduced set of interferometric SAR images. *IEEE Transactions on Geoscience and Remote Sensing*, *41*(10), 2243–2253. https://doi.org/10.1109/TGRS.2003.817018

Mosley, M. P. (1982). Analysis of the effects of changing discharge on channel morphology and instream uses in a braided river, Ohau River, New Zealand. *Water Resources Research*, *18*(4), 800–812. https://doi.org/10.1029/wr018i004p00800

Mosley, M. P. (1983). Response of braided rivers to changing discharge. *Journal of Hydrology*, *22*(1), 18–67.

Paola, C. (1996). Incoherent structure: Turbulence as a metaphor for stream braiding. In P. J. Ashworth, S. J. Bennet, J. L. Best, & S. J. McLelland (Eds.), *Chapter 33, Coherent flow structures in open channels*. John Wiley & Sons Ltd.

Paola, C. (2001). Modelling stream braiding over a range of scales. In M. P. Mosley (Ed.), *Gravel-Bed Rivers V*. Water Resources Publications, LLC.

Parker, G. (1979). Hydraulic geometry of active gravel rivers. *Journal of the Hydraulics Division*, *105*(HY9), 1185–1201. https://doi.org/10.1061/jyceaj.0005275

Parker, G., Wilcock, P. R., Paola, C., Dietrich, W. E., & Pitlick, J. (2007). Physical basis for quasi-universal relations describing bankfull geometry of single-thread gravel bed rivers. *Journal of Geophysical Research*, *112*, F04005.

Peirce, S., Ashmore, P., & Leduc, P. (2018). The variability in the morphological active width: Results from physical models of gravel-bed braided rivers. *Earth Surface Processes and Landforms*, *43*(11), 2371–2383. https://doi.org/10.1002/esp.4400

Peirce, S., Ashmore, P., & Leduc, P. (2019). Evolution of grain size distributions and bed mobility during hydrographs in gravel-bed braided rivers. *Earth Surface Processes and Landforms*, *44*(1), 304–316. https://doi.org/10.1002/esp.4511

Ragno, N., Redolfi, M., & Tubino, M. (2022). Quasi-universal length scale of river anabranches. *Geophysical Research Letters*, *49*(16), e2022GL099928. https://doi.org/10.1029/2022gl099928

Recking, A., Johannot, A., Horita, K., Melun, G., Vázquez-Tarrío, D., Zanker, S., et al. (2024). An attempt to take into account natural variability in 1D bedload prediction. *Journal of Geophysical Research: Earth Surface*, *129*(7), e2023JF007601. https://doi.org/10.1029/2023JF007601

Recking, A., Piton, G., Vazquez-Tarrio, D., & Parker, G. (2016). Quantifying the morphological print of bedload transport. *Earth Surface Processes and Landforms*, *41*(6), 809–822. https://doi.org/10.1002/esp.3869

Rhoads, B. L. (2020). *River dynamics. Geomorphology to support management*. Cambridge University Press.

Robertson-Rintoul, M. S. E., & Richards, K. S. (1993). Briaded-channel patterns and pleohydrology using an index of total sinuosity. In J. L. Best & C. S. Bristow (Eds.), *Braided Rivers* (Vol. 75, pp. 113–118). Geological Society Special Publication.

Rossi, D., Zolezzi, G., Bertoldi, W., & Vitti, A. (2023). Monitoring braided river-bed dynamics at the sub-event time scale using time series of Sentinel-1 SAR imagery. *Remote Sensing*, *15*(14), 3622. https://doi.org/10.3390/rs15143622

Rouse, J. W., Haas, R. H., Schell, J. A., & Deering, D. W. (1973). Monitoring vegetation systems in the Great Plains with ERTS. In *Proceedings of the 3rd Earth resources technology satellite symposium (10-14 December 1973)* (pp. 309–317). NASA SP-351, Goddard Space Flight Center.

Smith, C. L., Isacks, B. L., Bloom, A. L., & Murray, A. B. (1996). Estimation of discharge from three braided rivers using synthetic aperture radar satellite imagery: Potential application to ungagged basis. *Water Resources Research*, *32*(7), 2021–2034. https://doi.org/10.1029/96wr00752

Stecca, G., Hicks, D. M., Measures, R., & Henderson, R. (2023). Numerical modeling prediction of vegetation trajectories under different flow regimes in New Zealand braided rivers. *Journal of Geophysical Research: Earth Surface*, *128*(12), e2023JF007397. https://doi.org/10.1029/2023JF007397

Trampush, S. M., Hazurbazar, S., & McElroy, B. (2014). Empirical assessment of theory for bankfull characteristics of alluvial channels. *Water Resources Research*, *50*(12), 9211–9220. https://doi.org/10.1002/2014wr015597

Versace, P., Ferrari, E., Gabriele, S., & Rossi, F. (1989). *Valutazione delle piene in Calabria*. CNR-IRPI Geodata.

Viparelli, C. (1964). *Granulometria delle alluvioni dei torrenti calabresi*. Istituti Idraulici, Università di Napoli (in Italian).

Viparelli, C. (1972). Corsi d'acqua naturali e leggi che ne regolano il modellamento. *Quaderno No. 4: Istituto di Idraulica e Costruzioni Idrauliche. (in Italian)*.

Viparelli, C., & Viparelli, M. (1979). Studio Idrologico della Calabria Settentrionale. *Cassa per le Opere Straordinarie di Pubblico Interesse nell'Italia Meridionale. (in Italian)*.

Viparelli, E., & Eke, E. C. (2021). Equilibrium of self-formed, single-thread, sand-bed rivers. *Geophysical Research Letters*, *48*(20), e2021GL094591. https://doi.org/10.1029/2021gl094591

Warburton, J. (1996). Active braidplain width, bedload transport and channel morphology in a model braided river. *Journal of Hydrology*, *35*(2), 259–285.

Wilkerson, G. V., & Parker, G. (2011). Physical basis for quasi-universal relationships describing bankfull hydraulic geometry of sand-bed rivers. *Journal of Hydraulic Engineering*, *137*(7), 739–753. https://doi.org/10.1061/(asce)hy.1943-7900.0000352